AFOSR-TR- 80-0005

Air Force Office of Scientific Research
Grant AFOSR-76-3073

ADA079597

CURRENTS AND CHARGES ON CYLINDERS
IN A PARALLEL-PLATE TRANSMISSION LINE

LEVEL II

Gordon McKay Laboratory
Harvard University
Cambridge, MA 02138

July 1979

Final Report
June 30, 1976 through June 30, 1979

Approved for public release; distribution unlimited

D D C
RECEIVED
JAN 21 1980
D

Prepared for
AIR FORCE OFFICE OF SCIENTIFIC RESEARCH (AFSC)
Bolling Air Force Base
Washington, DC 20332

80   1   16   074

REPORT DOCUMENTATION PAGE	READ INSTRUCTIONS BEFORE COMPLETING FORM

1. REPORT NUMBER	2 GOVT ACCESSION NO.	3 RECIPIENT'S CATALOG NUMBER
AFOSR-TR- 80-0005		

4. TITLE (and Subtitle)	5. TYPE OF REPORT & PERIOD COVERED
CURRENTS AND CHARGES ON CYLINDERS IN A PARALLEL-PLATE TRANSMISSION LINE	Final Report June 30, 1976 – June 30, 1979
	6. PERFORMING ORG. REPORT NUMBER

7. AUTHOR(s)	8. CONTRACT OR GRANT NUMBER(s)
T. T. Wu, M. Krook, R. W. P. King, D. J. Blejer, T. K. Sarkar, S. K. Wan, M. Owens, B. H. Sandler, J. E. Baum, and M. J. Miller	AFOSR-76-3073

9. PERFORMING ORGANIZATION NAME AND ADDRESS	10. PROGRAM ELEMENT, PROJECT, TASK AREA & WORK UNIT NUMBERS
Harvard University Division of Applied Sciences Cambridge, Massachusetts 02138	9751 64711F

11. CONTROLLING OFFICE NAME AND ADDRESS	12. REPORT DATE
Air Force Office of Scientific Research/NP Bolling Air Force Base Washington, DC 20332	Jul 79
	13. NUMBER OF PAGES 83

14. MONITORING AGENCY NAME & ADDRESS(if different from Controlling Office)	15. SECURITY CLASS. (of this report)
	Unclassified
	15a. DECLASSIFICATION DOWNGRADING SCHEDULE

16. DISTRIBUTION STATEMENT (of this Report)

Approved for public release; distribution unlimited.

17. DISTRIBUTION STATEMENT (of the abstract entered in Block 20, if different from Report)

Final rept, 30 Jun 76 – 30 Jun 79,

Accession For

NTIS GRA&I [X]
DDC TAB
Unannounced
Justification

By
Distribution/
Availability Codes
Dist. Avail and/or special
A

18. SUPPLEMENTARY NOTES

19. KEY WORDS (Continue on reverse side if necessary and identify by block number)

Experimental study, model EMP simulator
Electric field in simulator, at two different high frequencies
Approximate theoretical representation; TEM, TM, and TE modes
Surface charge density distributions
Possible methods to improve field in simulator

20. ABSTRACT (Continue on reverse side if necessary and identify by block number)

The final report summarizes the results of a 3-year model study to evaluate how well a parallel-plate transmission-line structure simulates an electromagnetic pulse with a plane-wave front. The amplitude and phase of the electric field inside the model simulator have been measured at two high frequencies for which transmission-line theory does not apply. An approximate theoretical representation of the field is used to interpret the measured data. Differences between the actual field and the desired traveling plane-wave field are discussed, and possible methods to improve the field in the simulator are offered.

DD FORM JAN 73 1473 EDITION OF 1 NOV 65 IS OBSOLETE 457 000 UNCLASSIFIED

SUMMARY

In order to determine the magnitudes and distributions of currents and
charges induced on the surfaces of an aircraft when it encounters an
electromagnetic pulse generated by a nuclear explosion, large simulators
have been constructed in which the aircraft can be exposed to a hopefully
comparable electromagnetic environment. One important type consists of a
parallel-plate transmission line or open waveguide with tapered triangular
ends, between the conductors of which a pulse with a plane wave front must
travel. Since the relevant pulse contains a frequency spectrum with wave-
lengths that extend from very long to relatively short compared to the
dimensions of the aircraft, the separation of the two conductors of the
transmission-line simulator cannot be kept small compared to all of the
wavelengths in the pulse as required for TEM transmission without propagating
higher modes. It follows that TEM-mode transmission-line theory can be
applied only to the very low frequency part of the spectrum, for which $kh = 2\pi h/\lambda \ll 1$.

The properties of the simulator at higher frequencies are difficult to
determine accurately. One approach is to measure the electric field in a
model simulator at one or more of the relevant higher frequencies, and then
seek to interpret its distribution theoretically. This has been done in a
carefully designed model simulator at two operating frequencies, $f = 626.5$
MHz ($\lambda = 48$ cm) and $f = 264$ MHz ($\lambda = 113.6$ cm). When the frequency is so
high that kh is not small, as when $kh = 2\pi h/\lambda = 4.5\pi$ or $h = 2.25\lambda$ with $\lambda = 48$ cm and the height $h = 108$ cm, the electric field in the working volume is
much more complicated than at low frequencies. This is true to a lesser
degree when $kh = 1.32\pi$ or $h = 0.66\lambda$ for $\lambda = 113.6$ cm and $h = 75$ cm. Owing
to the wide spacing, most of the energy supplied by the generator is now
radiated into the surrounding space, and only a small fraction is dissipated
in the load. The structure is essentially an antenna and not a transmission
line.

Direct measurements have been made of both the amplitude and phase of
the vertical (E_z) and longitudinal (E_y) components of the electric field
throughout the working volume and adjacent regions of the simulator, and of
E_z on the surfaces of both conducting plates where $E_y = 0$. In order to

1

interpret the measured results, the field in the working volume has been represented approximately in terms of the mode theory of the infinite parallel-plate waveguide. For the operating wavelength $\lambda = 48$ cm, four modes are well above cut-off. These are the TEM, TM_{01}, TM_{02}, and TM_{03} modes. Comparisons with the measured data indicate that the assumed approximate representation of the field by the superposition of ideal parallel-plate modes is a good one throughout the working volume of the simulator. It is also evident that the total E_z differs greatly from the part contributed by the TEM mode alone. This is true particularly near the top, where the difference between the incident spherical wave in the sloping sections and the plane wave in the working volume is greatest. There is no difference on the ground plane. TE modes contribute only negligibly and are ignored.

The components E_z and E_y in the working volume and adjacent regions were also measured with $f = 264$ MHz when $h = 75$ cm $= 0.66\lambda$ and $\lambda = 113.6$ cm. Now only the TEM and TM_{01} modes are above cut-off; TE modes are neglected. As with the higher frequency and greater height h of the working volume, the approximate representation of E_z and E_y by TEM and TM_{0n} modes is quite satisfactory.

The differences between the actual electromagnetic field in the working volume of the model simulator and the desired traveling plane wave are significant when $h = 108$ cm $= 2.25\lambda$ with $f = 626.5$ MHz, and considerably larger when $h = 75$ cm $= 0.66\lambda$ with $f = 264$ MHz. In the first place, the component E_z of the electric field is not uniform in either the transverse or vertical directions; secondly, there is a component E_y; and thirdly, there is a significant standing wave. It follows that the electrical environment of a metallic obstacle placed in the working volume is necessarily quite different from what it would be if it were exposed to an incident plane wave. A sample set of measurements of the very sensitive charge density distribution on the surface of a tubular cylinder when located at the center of the working volume has been compared with earlier data taken at the same frequency and on the same cylinder when illuminated by a spherical wave. These are discussed in conjunction with theoretically determined distributions for an incident plane wave. The report closes with a discussion of possible methods of reducing the lateral and vertical nonuniformity of the field in the simulator as well as the standing-wave ratio.

CONTENTS

ILLUSTRATIONS

4

5

TABLES

SECTION I

INTRODUCTION

The purpose of an EMP simulator is to provide an electromagnetic environment that approximates a traveling electromagnetic pulse composed of a spectrum of frequencies extending from very low to moderately high. For each component frequency, the electromagnetic field is a plane wave with mutually perpendicular electric and magnetic vectors that satisfy the relation $\vec{E} = \vec{c} \times \vec{B}$, where $\vec{c}$ is in the direction of propagation. It has the magnitude $c = 3 \times 10^8$ m/sec. One type of structure that is designed to generate an approximation of such a field is the guided-wave simulator which ideally has the properties of a uniform transmission line for the TEM mode at sufficiently low frequencies. That is, it has a characteristic impedance that is independent of the frequency and position along the direction of propagation and it can be terminated to provide a pure traveling wave at every cross section. Unfortunately, it is not obvious nor easily proved that the electromagnetic field in an actual simulator adequately approximates the desired properties at any or all frequencies in the pulse. The geometries of the different structures in actual use are such that a rigorous, quantitatively accurate analysis is very difficult. It follows that recourse must be had in numerical investigations or in direct measurements. Actually, an accurate and complete experimental study of the electromagnetic field in the working volume of a guided-wave simulator is faced with many difficulties. It is the purpose of this final report to summarize the results of such a study performed on the model simulator at Harvard University and, in order to make them meaningful, to interpret the measurements with the help of approximate, but instructive, theoretical results.

SECTION II

THE HARVARD EMP SIMULATOR

A detailed experimental study has been made of the electric field in the guided-wave simulator shown schematically in Figures 1 and 2. It consists of a rectangular metal plate between sloping triangular plates supported over a large aluminum ground plane (7.93 × 3.35 m) by dielectric cables and styrofoam blocks. It is driven at one end by the vertical extension of the inner conductor of a coaxial line connected to a CW power oscillator. It is terminated at the other end in standard two-watt resistors in parallel. The three-dimensional region under the rectangular plate is called the working volume. Its length b is 115 cm, its width 2a is 175 cm. Its height h above the ground plane is adjustable with the help of hinged joints between it and the sloping triangular plates combined with movable feed and load points. Two heights and frequencies have been used. They are h = 108 cm with f = 625 MHz or λ = 48 cm so that h/λ = 2.25, and h = 75 cm with f = 264 MHz or λ = 113.6 cm so that h/λ = 0.66. The altitude of each of the identical triangular plates is 331 cm and their projections on the ground plane when h = 108 cm are 311.5 cm, when h = 75 cm the projections are 322 cm. These dimensions provide a characteristic impedance of 100 Ω when h = 108 cm, of 80 Ω when h = 75 cm. A small corner reflector is placed behind the driven end; absorbing material completely surrounds the edges of the ground plane.

Cartesian coordinates are used to describe the location of a point in and near the working volume of the simulator. The origin is on the ground plane directly below the center of the parallel plate. The unit vectors $\hat{x}, \hat{y}, \hat{z}$ define, respectively, the transverse, longitudinal, and vertical directions, as indicated in Figure 2. Note that $\hat{y}$ points in the direction of propagation. For preliminary measurements the spherical coordinates (r, ϕ, θ) are also used with the origin (r = 0) on the ground plane at the driving point (see Figure 9). When h = 108 cm, the load is at (r, ϕ, θ) = (738, 90°, 0°), where r is in centimeters.

In order to determine the electric field in the working volume and in the adjacent sections of the pyramidal regions as well as along the surfaces of the ground plane and the upper parallel plate, a system of movable probes

10
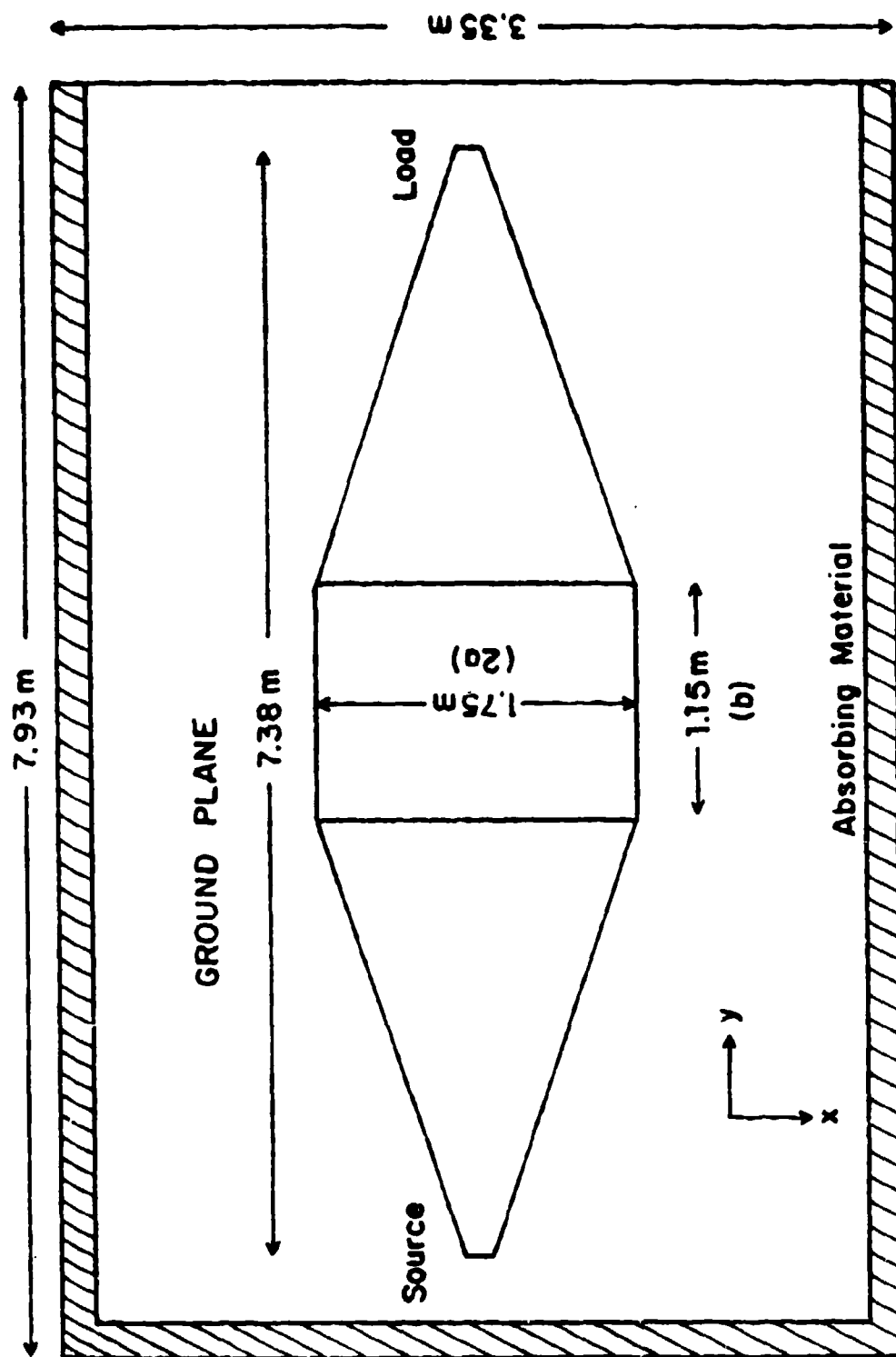
FIG. 1 TOP VIEW OF SIMULATOR SETUP

FIG. 2 SIMULATOR WITH ① GROUND-PLANE PROBE, ② TOP-PLATE PROBE, ③ SPACE PROBE IN WORKING VOLUME.

was designed and constructed for the direct measurement of both the amplitude and phase of E_y and E_z. As explained later, a small component E_x exists primarily near the open sides where fringing occurs, but this could not be measured. The component E_z on the ground plane was measured with a monopole probe 4 cm long, mounted on a brass disk 10 cm in diameter, and designed to slide along the ground plane when moved by means of a pulley system. The probe cable was constrained to lie flat on the ground plane and was, therefore, always perpendicular to the electric field. The measurement of E_z on the underside of the upper parallel plate was accomplished with a monopole probe that projects down into the working volume through longitudinal slots cut into the parallel plate. The probe was mounted on a brass block which was machined to slide in the slots. The output cable from the base of the probe was placed in a shielding tube constructed to lie along the upper surface of the sloping triangular plate leading to the load. The cable in its shielding tube extended beyond the load parallel to the ground plane and over its edge to the instrumentation below, as shown in Figure 2. The section over the ground plane constituted a transmission line with a character-istic impedance of 100 Ω. It was short-circuited at a distance of $\lambda/4$ from the load by a metal plate and so acted like an open circuit at the load.

The electric field throughout the working volume was measured with a dipole antenna that could be oriented vertically to measure E_z and hori-zontally to measure E_y. It was continuously movable in the working volume and adjacent sections below the triangular plates. The probe cable consisted of twin coaxial lines that were held parallel to the transverse x-axis as the probe was moved. This assured that they were perpendicular to both E_z and E_y, but necessarily parallel to E_x - which could excite axial standing-wave distributions of current and charge on their surfaces. Since these would have a charge maximum at the end adjacent to the terminals of the dipole, they could induce an undesired voltage across them if complete geometrical symmetry did not obtain. No such difficulty was encountered with f = 626.5 MHz, and the simple space probe (a) shown in Figure 3 was used to measure E_z and E_y throughout the working volume. At f = 264 MHz, an undesired voltage due to E_x was observed - presumably because the long twin cables from the probe in the working volume to the vector voltmeter under the ground plane happened to be near a resonant length. This difficulty was avoided by enclosing the twin cables in a metal tube provided

13
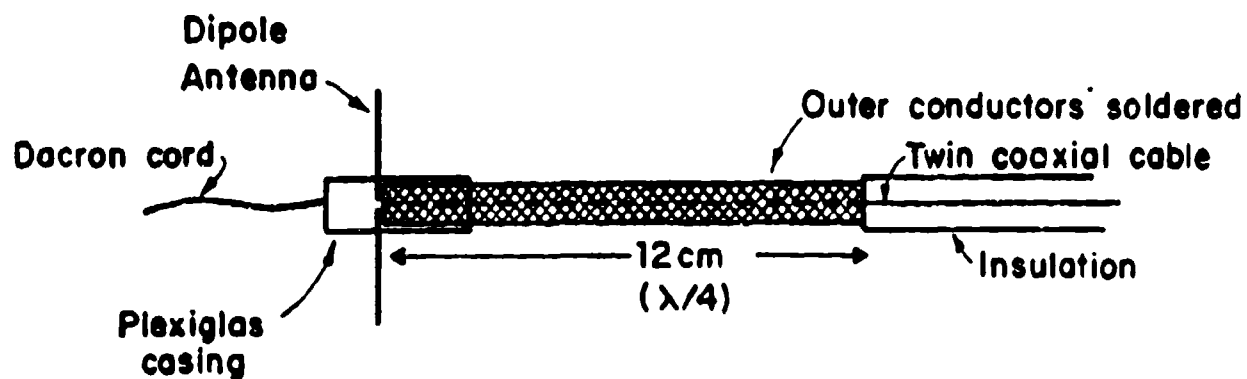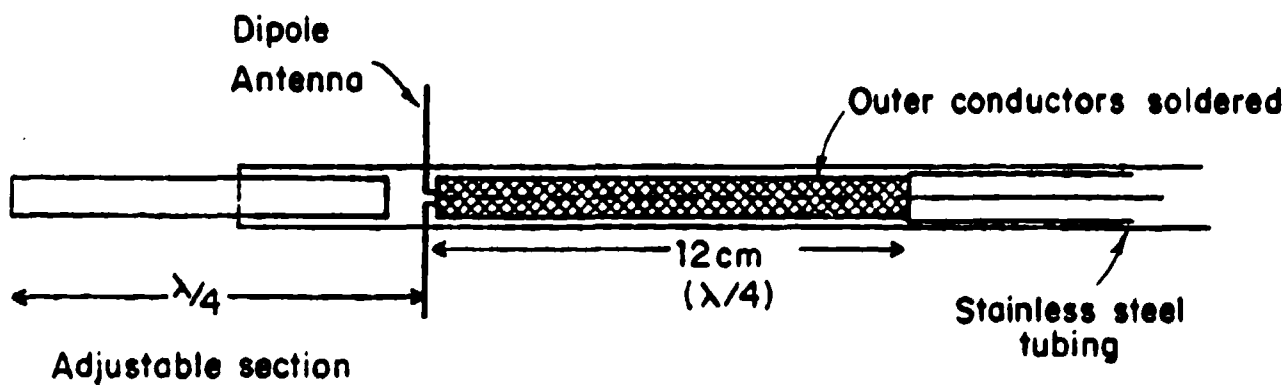
SPACE PROBE (a)

SPACE PROBE (b)

FIG. 3 DIAGRAMS OF SPACE PROBES

14

with an adjustable extension beyond the dipole, as shown in the diagram for space probe (b) in Figure 3. When the extension was adjusted to a quarter wavelength, the dipole was located at a charge minimum, instead of a charge maximum, in any standing wave induced on the tube by E_x. The undesired voltage across the terminals of the evidently not perfectly symmetrical dipole was thus reduced to an unobservable value.

SECTION III

PRELIMINARY MEASUREMENTS

Before measurements were made in the model simulator, the standing-
wave pattern on the ground plane with its surrounding absorbing walls was
investigated. The source was a short monopole at the location of the
driving-point of the simulator (r = 0), backed by a small corner reflector.
The frequency was f = 626.5 MHz or λ = 48 cm. By means of the movable
monopole probe, the electric field E_z along the radial line θ = 0° was
measured in both amplitude and phase, as shown in Figure 4 in solid lines.
It corresponds to the spherical traveling wave $E_z = Ae^{ikr}/r$ with a super-
imposed standing-wave ripple. In order to determine the predominant cause
of the reflections that generate the standing wave, a reflecting plane was
placed successively in three positions. For the first location normal to
the direction of propagation at r = s = 606 cm, the field distribution shown
in Figure 4 in dotted lines was obtained. This resembles the graphs in
solid line, but with a substantially higher standing-wave ratio. For the
second location, the reflecting plate was moved away from the source a
distance of one quarter wavelength to s = 618 cm. The new field distribution
was like the dotted one in Figure 4, but with the entire standing-wave
pattern moved away from the source a distance of a quarter wavelength. A
theoretical curve for the field when the reflecting plane at s = 606 cm is
infinite in extent is shown in Figure 5 for comparison with the measured
dotted graphs in Figure 4. The third location of the reflecting plane was
normal to the x-direction and flat against the absorbing material on one
side at x = -136 cm. The field measured in this case differed negligibly
from that in the absence of any reflecting plane, shown in solid lines in
Figure 4. These tests indicate that the reflections that produce the small
standing wave shown by the solid-line graphs in Figure 4 originate at the
rear edge and wall of the absorbing material. Their small amplitude shows
that while there is some reflection from the edge of the ground plane and
the absorbing material, this latter is generally effective in providing a
predominantly traveling wave that closely approximates that over a plane of
infinite extent.

The next set of preliminary measurements was carried out with the
parallel rectangular and sloping triangular plates of the simulator in place,

16
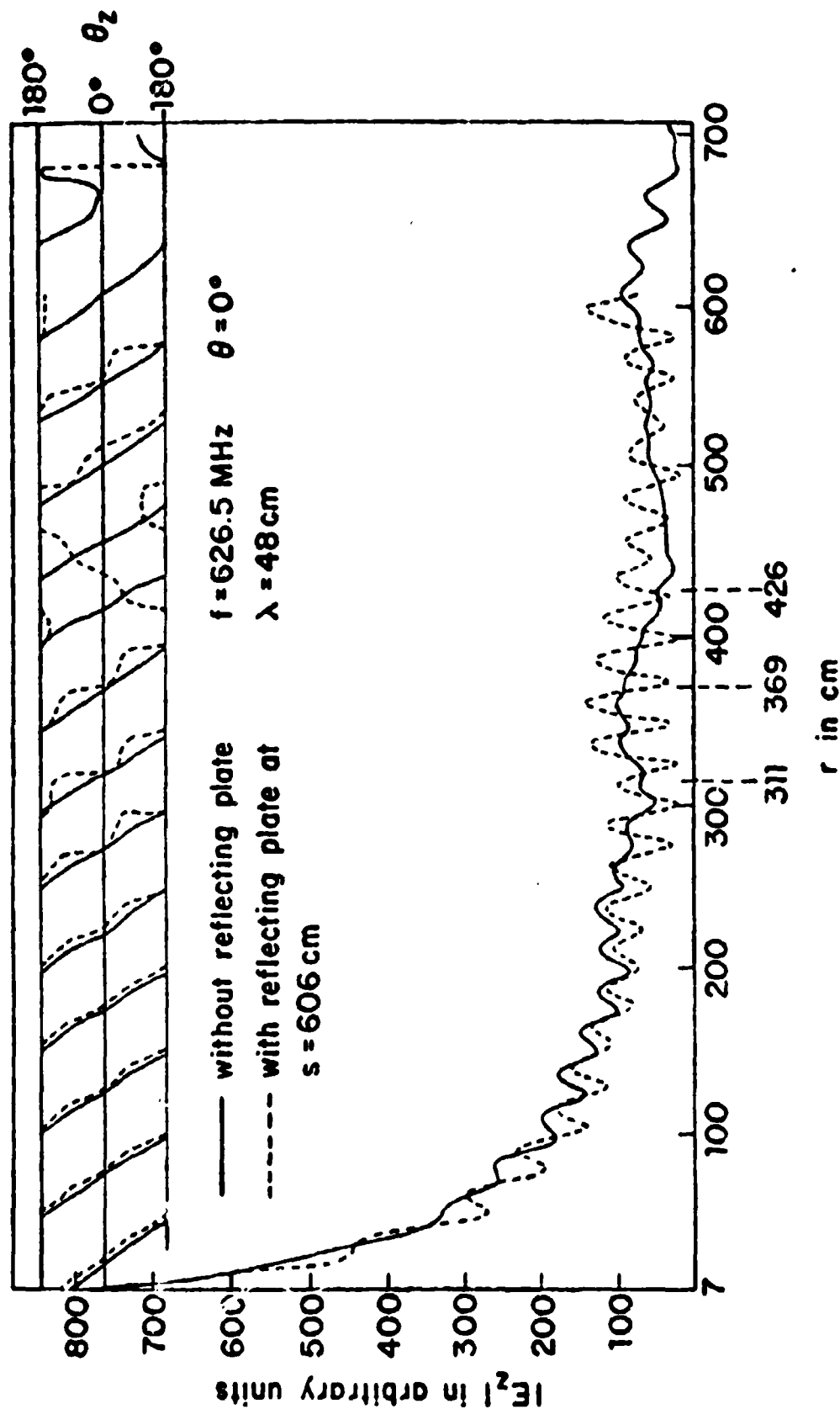
Fig. 4   Measured E_z along $\theta = 0°$ on ground plane excited by monopole and corner reflector.

Source at r = 0
Reflecting plane at $s = 606$ cm
$\lambda = 48$ cm
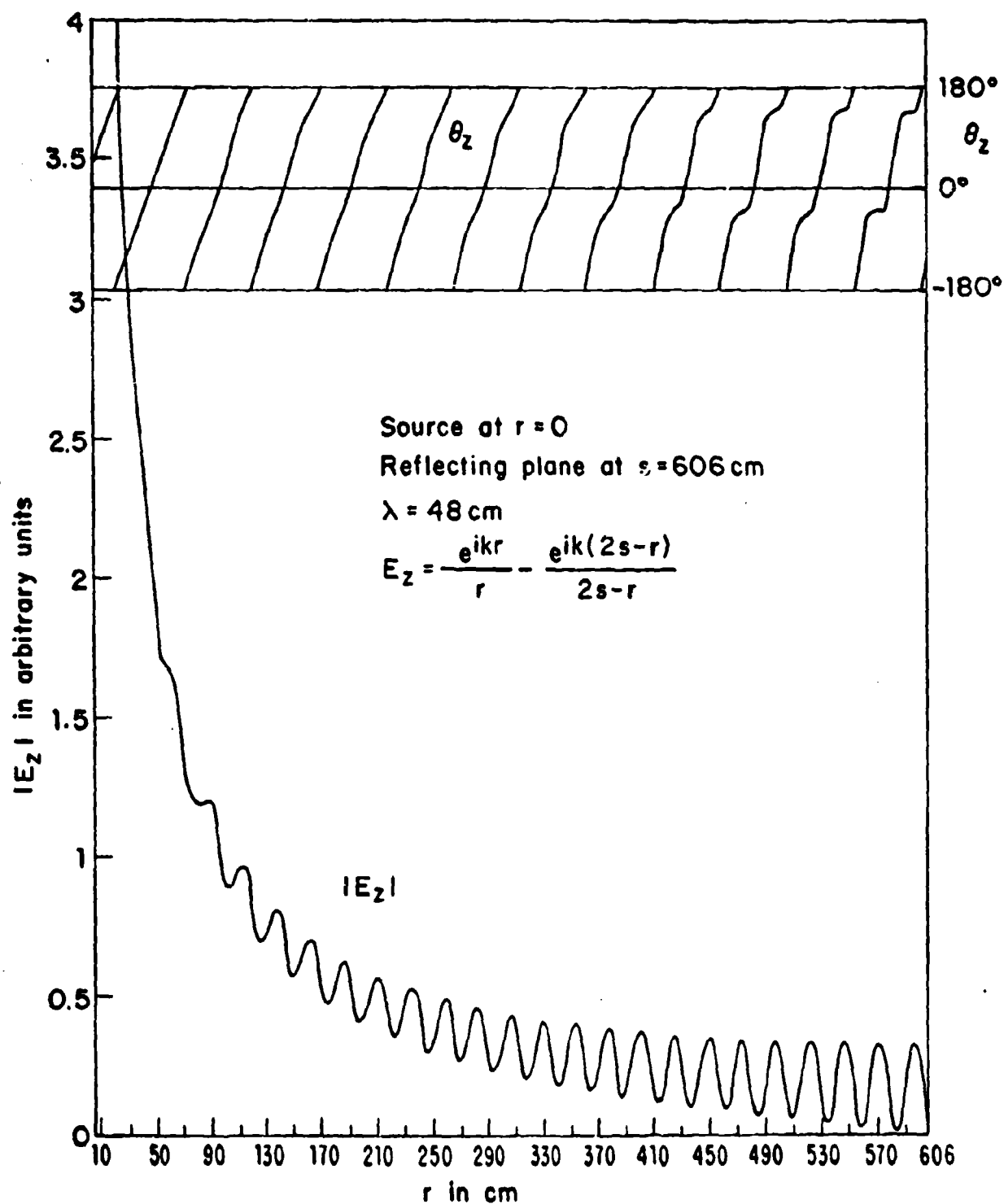$$E_z = \frac{e^{ikr}}{r} - \frac{e^{ik(2s-r)}}{2s-r}$$

$|E_z|$

Fig. 5 Theoretical electric field along $\theta = 0°$ on ground plane for comparison with measured graphs in Fig. 4.

and with a load of 105 Ω as the termination. This value was chosen after measurements showed that it provided the lowest standing-wave ratio in the region near the load. Graphs of $|E_z|$ and θ_z are shown in Figure 6 for a distance of more than a wavelength adjacent to the 105 Ω load. The standing-wave ratio of 3.7 shows that there is substantial reflection even with the best matched load. (It should be added that no really significant change in the standing-wave ratio was observed when the load was varied widely above and below 105 Ω.) In Figure 7 are shown the graphs of $|E_z|$ and θ_z along the ground plane corresponding to those in solid lines in Figure 4, but now with the simulator plates in place. There is no dramatic difference. The main outline is still that of a traveling spherical wave with a superimposed standing wave. The latter is somewhat reduced near the source, somewhat enhanced near the load.

In Figure 8 are graphs in (a) of the measured phase fronts of E_z on the ground plane at four different radial distances between the source and the beginning of the working volume at y = -57.5 cm (r = 311.5 cm, θ = 0°). They are seen to be essentially circular with small oscillations near θ = 15° due to edge effects from the sloping triangular plate above. The same information is conveyed in a different manner in (b) of Figure 8 which shows the phase along the line y = -265 cm between x = 0 and x = -114.5 cm. The solid line shows the measured phase, the broken line the theoretical phase for an ideal spherical wave with the wavelength λ = 47.88 cm. A graph of $|E_z|$ along a circular arc r = 55 cm is shown in (c) of Figure 8. It is constant within 1 dB under the sloping triangular plate where $0 \le \theta \le 15°$. In the region beyond the projection of the edge of the triangular plate, i.e., $15° < \theta \le 30°$, $|E_z|$ varies within a 3 dB range. It follows from Figure 7 that in the region beyond five wavelengths from the source, but not as far as the rear triangular plate, i.e., $250 \le r \le 400$ cm, $|E_z|$ is fairly constant in magnitude but with a superimposed standing-wave ripple. In this range the standing-wave ratio is relatively small, and the phase reasonably linear. Beyond the parallel-plate region, r > 426 cm, the standing-wave ratio is much higher, and the phase departs substantially from the linear.

It may be concluded from these preliminary measurements of E_z along the ground plane, that the field incident on the parallel-plate region is essentially a traveling spherical wave with a superimposed standing wave of relatively small amplitude.
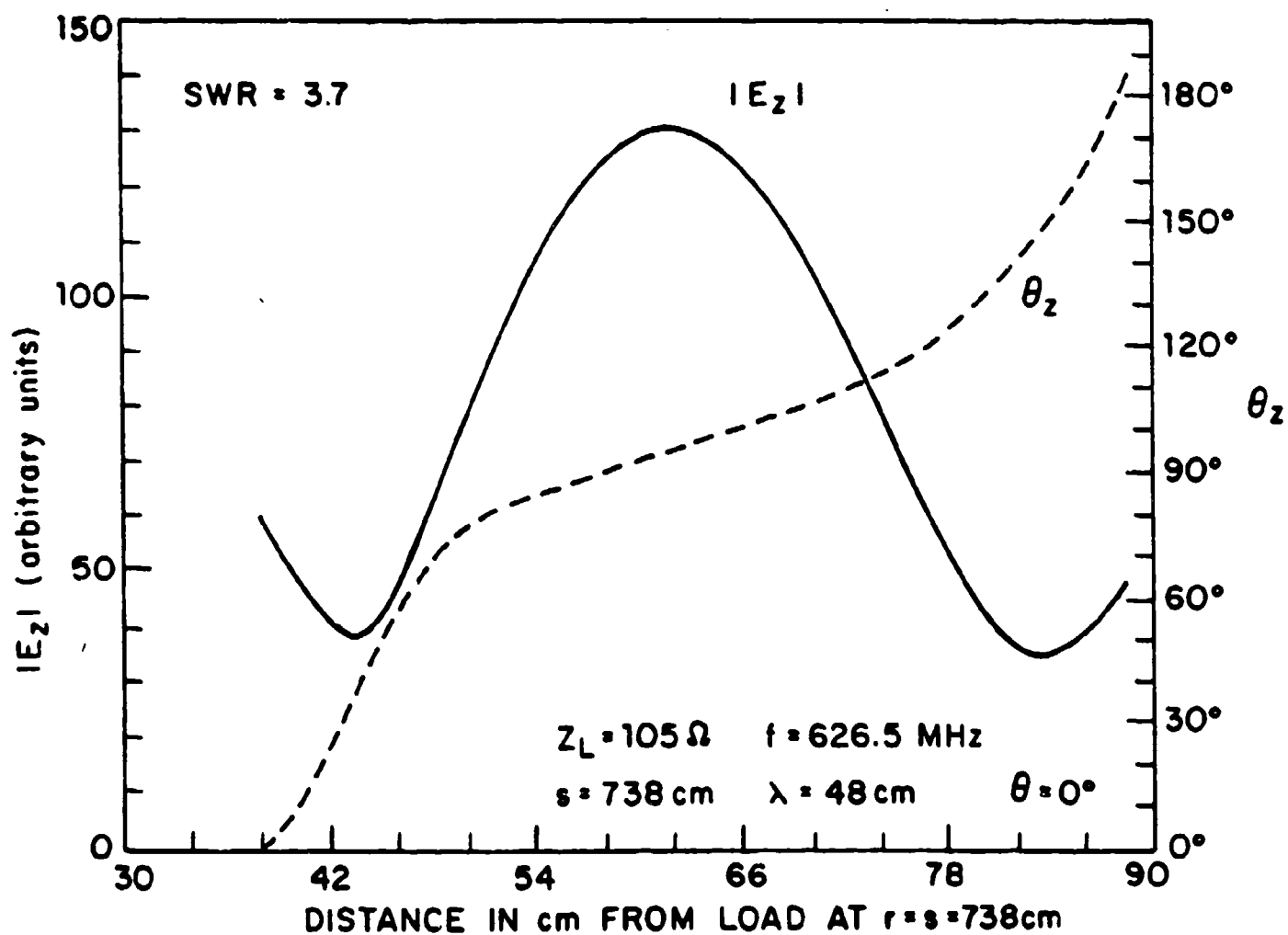
19

FIG. 6 STANDING WAVE OF |Eᵤz| NEAR LOAD
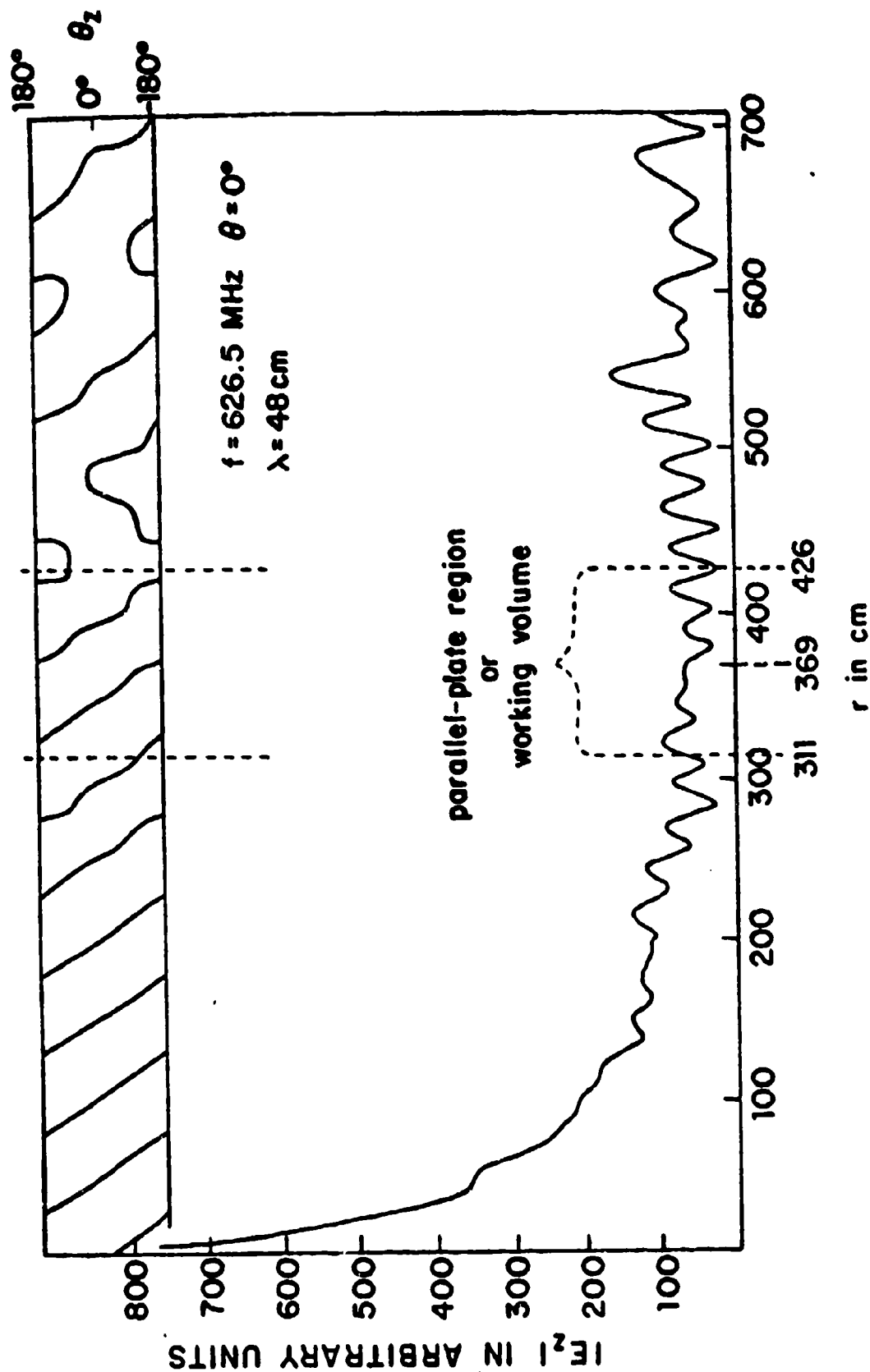
FIG. 7 MEASURED E_z ALONG $\theta = 0°$ OF GROUND PLANE OF TERMINATED SIMULATOR
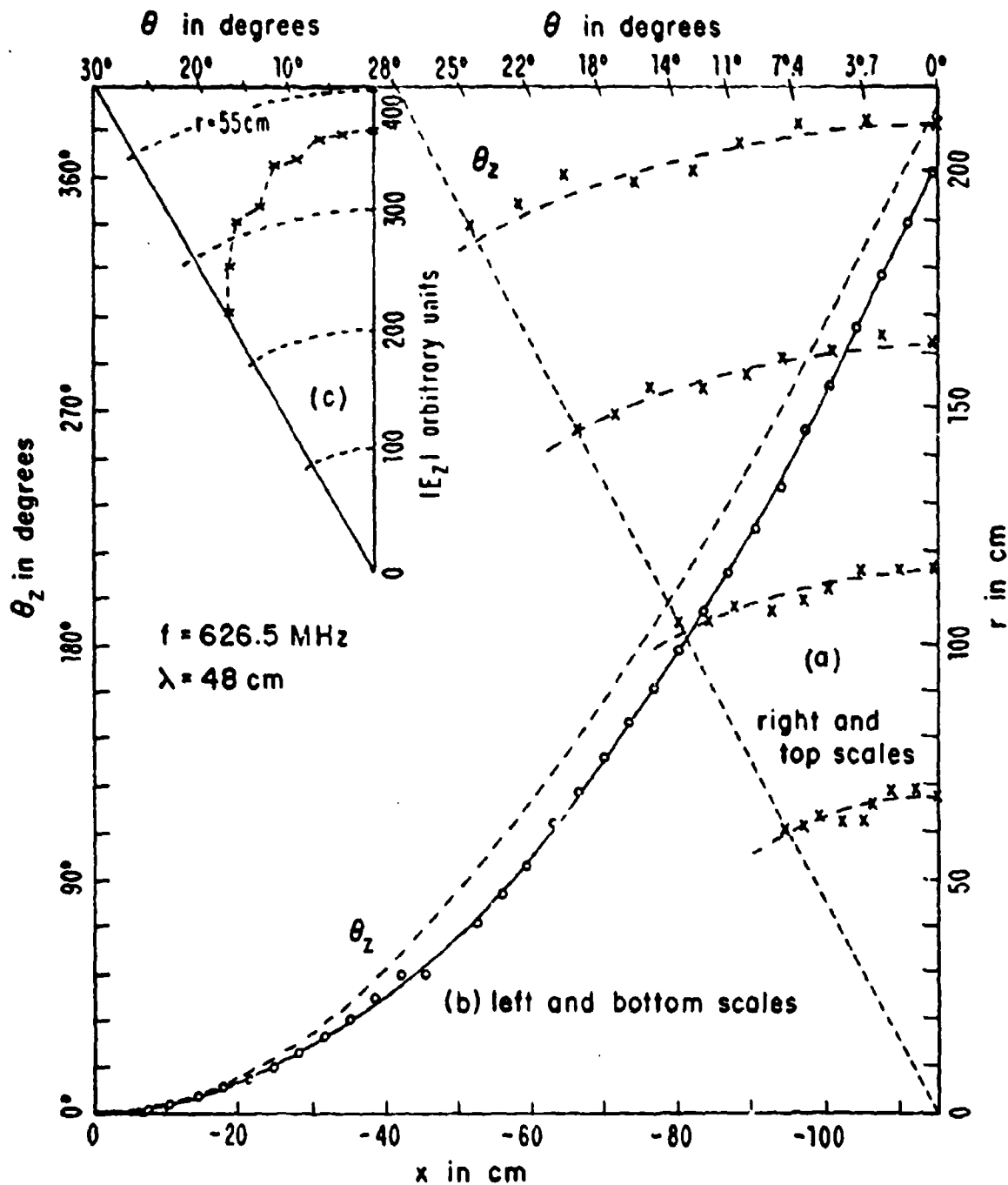
Fig. 8 (a) Measured phase fronts in the simulator; (b) Phase angle θ_z along the line y = -265 cm; (c) $|E_z|$ at r = 55 cm from the source.

SECTION IV

INTRODUCTORY DESCRIPTION OF THE FIELD IN THE WORKING VOLUME

In order to provide a meaningful set of measurements of the electro-
magnetic field in the working volume of the simulator, that is, in the
parallel-plate region and adjacent sections of the tapered ends, it is
necessary to review briefly the elementary theoretical foundations.
Consider first the field at frequencies that are sufficiently low to make
the height h a negligible fraction of a wavelength, i.e., $kh = 2\pi h/\lambda \ll 1$.
In this important range, the entire structure has the properties of an end-
loaded transmission line operating in the TEM mode with negligible radiation,
low line losses, a constant characteristic impedance, and a standing-wave
ratio determined by the terminating load impedance. The TEM electric field
in the working volume is vertically directed and approximately independent
of the transverse coordinates x and z at points not too close to the side
edges of the plates where fringing effects occur. That is, $\vec{E}(x,y,z) \doteq$
$\hat{z}E_z(y)$. $E_z(y)$ is proportional to $V(y)$, the transmission-line voltage across
the conductors. The planes y = constant are ideally surfaces of constant
amplitude $|E_z|$ and phase θ_z. The incident wave travels in the positive
y-direction, the reflected wave in the negative y-direction. With a proper
termination $Z_L = Z_c$, the reflected wave from the load can be reduced to a
negligible value. However, reflections do take place at the discontinuities
at the junctions of the parallel plate and the sloping triangular end plates.

When the frequency is so high that kh is not small, in particular, when
$kh = 2\pi h/\lambda = 4.5\pi$ or $h = 2.25\lambda$ as for the Harvard simulator at the operating
wavelength $\lambda = 48$ cm and the height $h = 108$ cm, the electric field in the
working volume is much more complicated. This is true to a lesser degree
when $kh = 1.32\pi$ or $h = 0.66\lambda$ as for the Harvard simulator when $\lambda = 113.6$ cm
and $h = 75$ cm. Owing to the wide spacing, most of the energy supplied by
the generator is now radiated into the surrounding space, and only a small
fraction is dissipated in the load. The structure is essentially an antenna
and not a transmission line. This has been confirmed by K. M. SooHoo (ref. 1)
in a numerical analysis of a comparable simulator. He concludes that in the
high-frequency region, the radiated power approaches 80% of that supplied by
the generator.

23

In order to understand the characteristics of the measured field and to relate them to the simple TEM field that dominates at low frequencies, it is advantageous to have an at least approximate theoretical representation of the field in the working volume. Owing to its finite size and connection to the sloping triangular driving and loading members, the working volume is not simply a section of an ideal parallel-plate waveguide of infinite length. No general analytical treatment of the complete simulator has been made. Analyses are available of infinitely long, parallel-plate waveguides with plates that have a finite width that is arbitrary (refs. 2 and 3), or that is very narrow (ref. 4), very wide (refs. 5 and 6), or infinitely wide (ref. 7). None of these provides any information on the fields in and the transmission-line properties of the long sloping triangular sections or of the junction region between them and the parallel-plate region. Unfortunately, they also provide primarily qualitative information about the fields in the parallel-plate section since this is only 115 cm long, but 175 cm wide and (with image) 216 cm (or 150 cm) high. Thus, the condition of infinite length (or at least great length compared with the transverse dimensions) implicit in all of the analyses of parallel-plate waveguides is not satisfied. Indeed, the parallel-plate section is relatively so short that end effects can be expected to be significant over much of its length. Even so, the theoretical representation of the field in an ideal parallel-plate waveguide in terms of propagating TEM, TM, and TE modes should provide the best available framework for interpreting the measured field in the working volume of the model simulator. Instead of reviewing these in general, it is expedient first to study the nature of the incident field in order to determine which of the many possible modes can actually be expected to be excited.

As has been demonstrated, the field incident on the parallel-plate region is essentially a spherical wave originating at the source with an electric field E_ϕ and magnetic field $H_\theta = B_\theta/\mu_0$ tangent to the surface of a sphere, as shown in Figure 9(a). The intersection of the spherical wave fronts with a vertical plane is shown in Figure 9(b). At points on the plane y = constant, $E_z = -E_\phi \sin \phi$, $E_y = E_\phi \cos \phi$. On the ground plane, $z = 0$ and $\phi = 90°$ so that $E_z = -E_\phi$ and $E_y = 0$. Thus, along the plane corresponding to the input surface $y = -57.5$ cm of the working volume, there is a vertical component E_z of the electric field and also a longitudinal component E_y which increases from zero at the ground plane to a maximum at
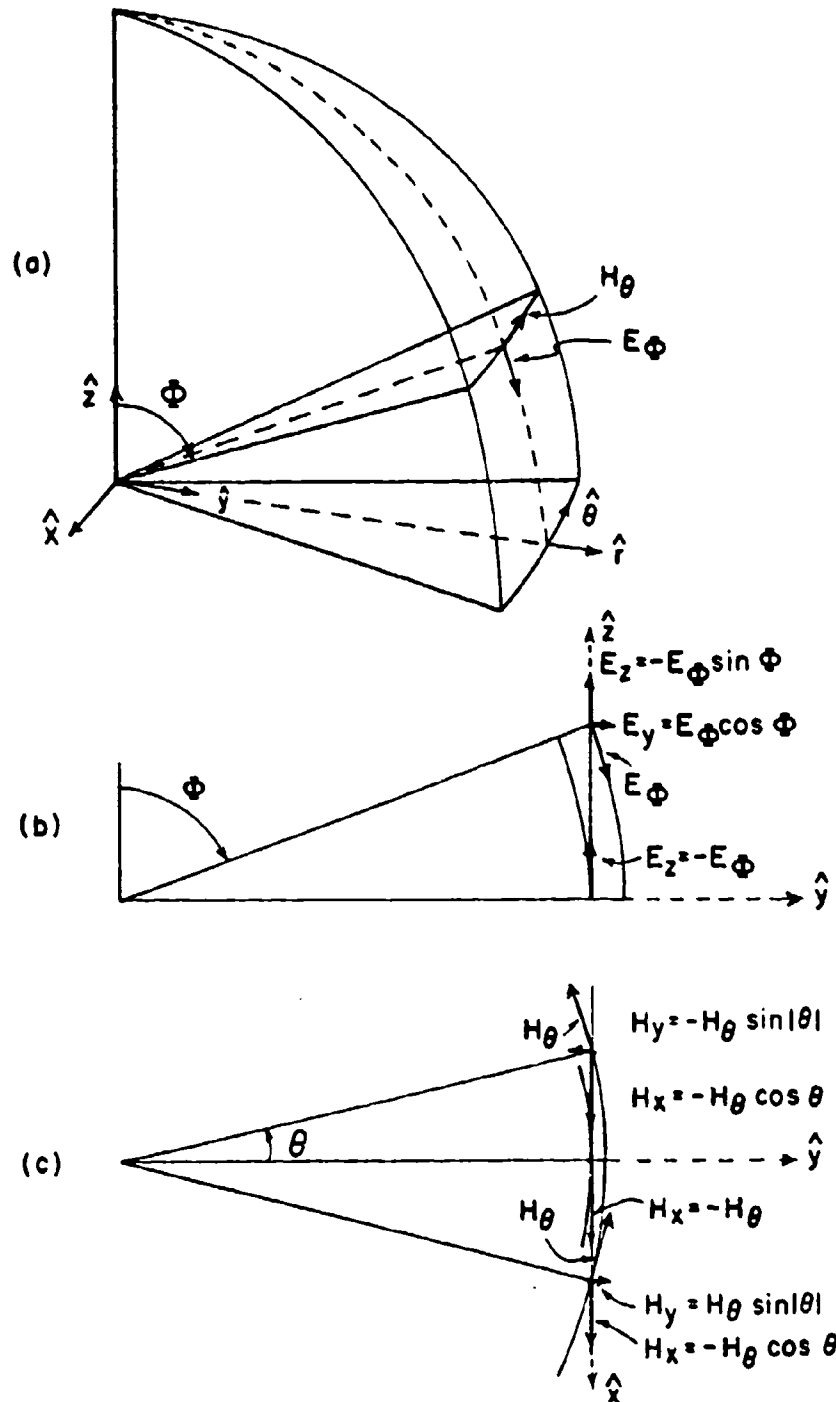
FIG. 9 SCHEMATIC DIAGRAMS OF SPHERICAL WAVE INCIDENT
ON A PLANE.(a) THREE DIMENSIONAL VIEW (b) ELECTRIC
FIELD IN VERTICAL PLANE (c) MAGNETIC FIELD IN
HORIZONTAL PLANE.

25

the top plate. In the parallel-plate region these components can excite the TEM mode and those TM modes that are symmetric with respect to the transverse z coordinate.

The intersection of the spherical wave with a vertical plane in a horizontal section is shown in Figure 9(c). At points along the plane $y =$ constant, $H_x = -H_\theta \cos \theta$, $H_y = -H_\theta \sin \theta$; at $x = 0$ and $\theta = 0°$, $H_x = -H_\theta$ and $H_y = 0$. Therefore, along the plane surface corresponding to the input surface $y = -57.5$ cm of the working volume, there is a transverse component H_x of the magnetic field and a longitudinal component H_y. The latter vanishes at $\theta = 0°$, is positive for $\theta < 0°$, negative for $\theta > 0°$. In the parallel-plate region, these components are associated with the TEM mode and those TE modes that are antisymmetric with respect to the transverse x coordinate. Thus, E_z may include components in the TEM, TM, and TE modes, E_y consists exclusively of TM modes, and E_x may be composed of both TM and TE modes. Similarly, H_x ~ ~ ·lude components in the TEM, TM, and TE modes, H_y consists exclusively of ·· modes, and H_z may be composed of both TE and TM modes.

SECTION V

THE FIELD IN THE PARALLEL-PLATE SECTION; TEM AND TM MODES

Since the field incident on the parallel-plate section of the simulator
is a spherical wave, it is of interest to determine the nature of the phase
fronts which characterize the electromagnetic field in that section. Measured
graphs of the wave fronts or contours of constant phase, θ_z = constant, of
the vertical component E_z of the electric field in the parallel-plate region
when h = 108 cm and f = 626.5 MHz are shown in Figures 10a and 10b in vertical
yz planes at discrete values of x ranging from x = 1.7 cm near the center at
x = 0 to x = -70.3 cm near the edge at x = -87.5 cm. Also shown are the wave
fronts of a spherical wave originating at the driving point (x = 0, y = -369
cm, z = 0). Clearly the phase fronts throughout the parallel-plate region
are essentially spherical with a superimposed oscillation due to reflections
from the top plate.

It is not convenient to describe the field in a parallel-plate wave-
guide in terms of spherical wave fronts originating at an outside point.
The natural representation is in terms of a superposition of plane waves
known as parallel-plane modes. The simplest form is given by the mode theory
of infinite parallel planes (ref. 7). Applicable to the parallel-plate
section of the simulator are the TM modes symmetric in z supplemented, if
desired, with the more complicated theory for plates of finite width (refs.
2 through 6). The significance of TE modes is considered in a later section.
The relevant TM modes are given by:[*]

$$E_{yn} = -i\zeta I_n(y)(n\lambda/2h)(\epsilon_n/h)^{1/2}\sin(n\pi z/h) \tag{1}$$

$$E_{zn} = -V_n(y)(\epsilon_n/h)^{1/2}\cos(n\pi z/h) \tag{2}$$

$$H_{xn} = I_n(y)(\epsilon_n/h)^{1/2}\cos(n\pi z/h) \tag{3}$$

where n = 0, 1, 2, ...; $\zeta = (\mu/\epsilon)^{1/2}$; ϵ_n = 1 when n = 0, ϵ_n = 2 when n ≠ 0.

---

[*]When referred to the full height with image, h is replaced by 2h, and n = 0,
2, 4, 6, ..., instead of 0, 1, 2, 3, ...
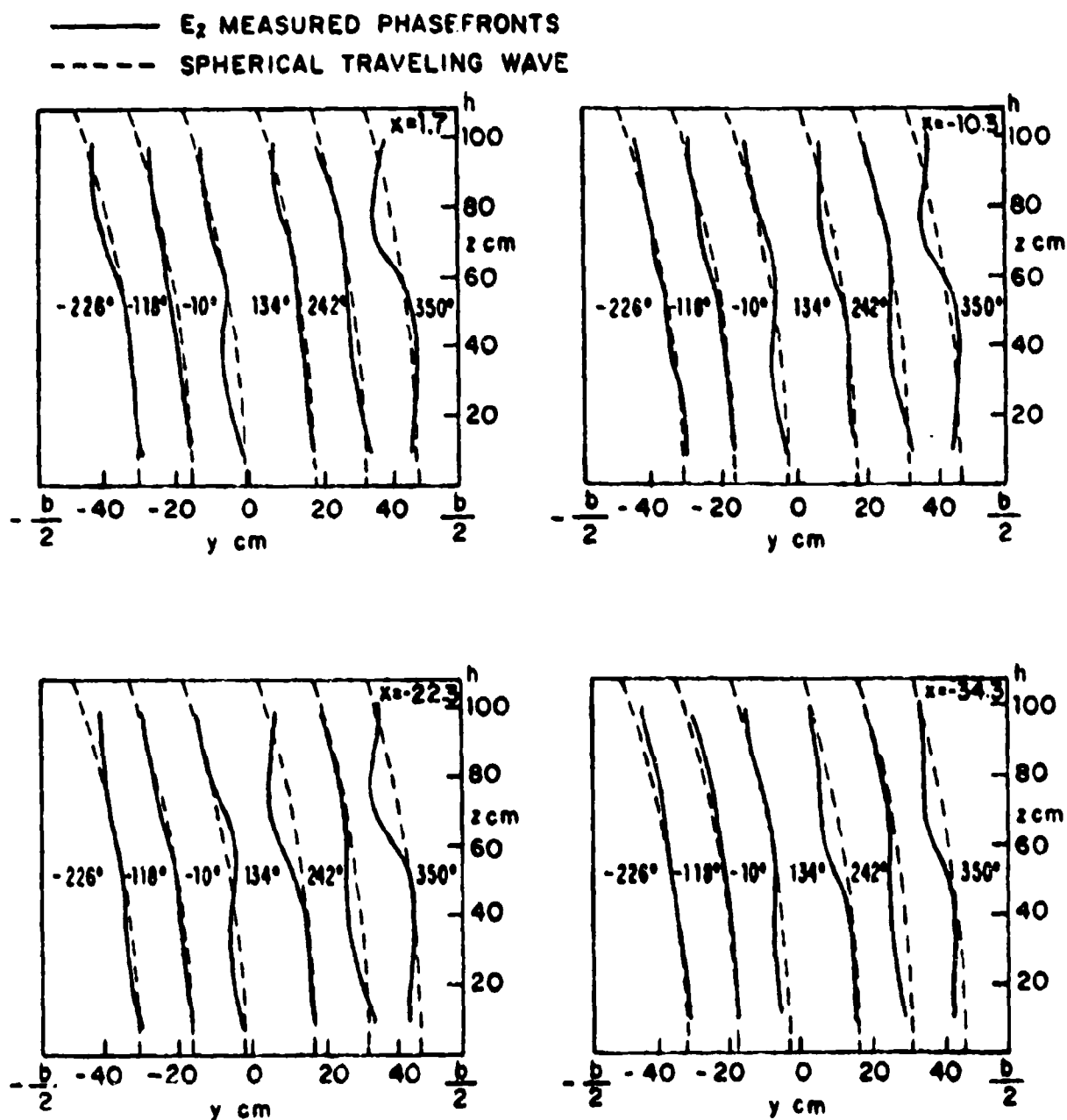
FIG. 10o MEASURED CONSTANT PHASE CURVES IN THE WORKING VOLUME;
h = 108 cm, b = 114.8 cm, f = 626.5 MHz

E₂ MEASURED PHASEFRONTS
—————— SPHERICAL TRAVELING WAVE
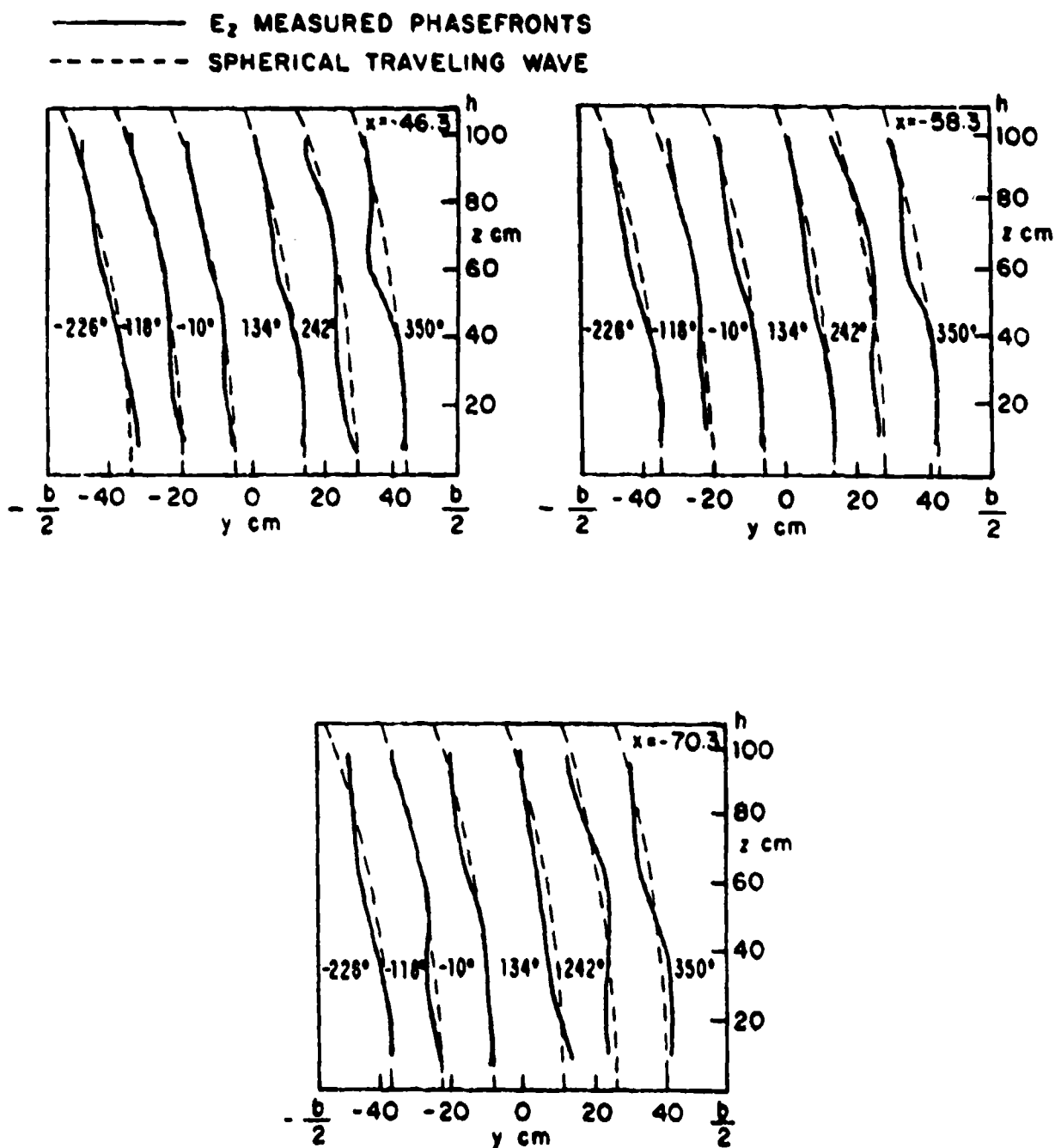
FIG. 10b MEASURED CONSTANT PHASE CURVES IN THE WORKING VOLUME;
h = 108 cm, b = 114.8 cm, f = 626.5 MHz

29

The generalized voltage and current functions $V_n(y)$ and $I_n(y)$ satisfy the simple transmission-line equations:

$$\frac{dV_n(y)}{dy} = ik_{gn}Z_{cn}I_n(y) \tag{4}$$

$$\frac{dI_n(y)}{dy} = ik_{gn}Y_{cn}V_n(y) \tag{5}$$

where the guide wave number k_{gn} and characteristic impedance Z_{cn} are:

$$k_{gn} = (k^2 - k_{cn}^2)^{1/2} \quad , \quad Z_{cn} = Y_{cn}^{-1} = \zeta k_{gn}/k \tag{6}$$

and the cut-off wave number k_{cn} is:

$$k_{cn} = 2\pi/\lambda_{cn} \quad , \quad \lambda_{cn} = 2h/n \tag{7}$$

The guide wavelength is $\lambda_{gn} = 2\pi/k_{gn}$. The voltage and current functions for the TM_{0n} modes in the parallel-plane section, -57.5 cm $\leq y \leq 57.5$ cm, can be represented as the sums of incident and reflected waves, i.e.,

$$V_n(y) = V_n^{inc}(0)e^{ik_{gn}y} + V_n^{ref}(0)e^{-ik_{gn}y} \tag{8}$$

$$I_n(y)Z_{cn} = V_n^{inc}(0)e^{ik_{gn}y} - V_n^{ref}(0)e^{-ik_{gn}y} \tag{9}$$

where $V_n^{inc}(0)$ and $V_n^{ref}(0)$ are the complex amplitudes of the incident and reflected voltage waves in the transverse plane $y = 0$.

For the Harvard working volume and with the operating frequency at $f = 626.5$ MHz, the TEM mode with $n = 0$ and three TM_{0n} modes with $n = 1, 2, 3$ can propagate. For the TEM mode, $k = k_{g0} = 0.1309$ cm^{-1}, for the TM_{0n} modes, $k_{g1} = 0.977k = 0.128$ cm^{-1}, $k_{g2} = 0.893k = 0.117$ cm^{-1}, and $k_{g3} = 0.748k = 0.098$ cm^{-1}. The corresponding guide wavelengths are $\lambda = \lambda_{g0} = 48$ cm for the TEM mode and $\lambda_{g1} = 49.1$ cm, $\lambda_{g2} = 53.7$ cm, and $\lambda_{g3} = 64.2$ cm for the TM_{0n} modes. The fields for the four modes are:

TEM: $\qquad E_y = 0 \quad , \quad E_z = 0.096 V_0(y) \quad , \quad H_x = 0.096 I_0(y)$ (10)

TM_{01}: $\quad E_y = -111.4 I_1(y) \sin(.029z) \quad , \quad E_z = -0.136 V_1(y) \cos(.029z)$

$$H_x = 0.136 I_1(y) \cos(.029z)$$ (11)

TM_{02}: $\quad E_y = -122.8 I_2(y) \sin(.058z) \quad , \quad E_z = -0.136 V_2(y) \cos(.058z)$

$$H_x = 0.136 I_2(y) \cos(.058z)$$ (12)

TM_{03}: $\quad E_y = -134.2 I_3(y) \sin(.087z) \quad , \quad E_z = -0.136 V_3(y) \cos(.087z)$

$$H_x = 0.136 I_3(y) \cos(.087z)$$ (13)

The relative amplitudes of the incident and reflected waves for each of these modes are not readily determined analytically. However, they can be estimated at any cross section of the working volume by comparison with the measured field.

The electric field lines characteristic of the TEM and first three TM_{0n} modes are shown in the yz-plane in Figure 11. At the upper left are the exclusively vertical field lines of the TEM mode. They have alternate upward and downward maxima at intervals of $\lambda/2 = 24$ cm. Note that there is no associated component E_y. At the upper right are the electric field lines for the TM_{01} mode. These resemble the TEM mode near the top conductor, but are oppositely directed near the ground plane since they are parts of closed loops with an E_y component in the region halfway between the conducting surfaces. The alternating upward and downward maxima now occur at intervals of $\lambda_{g1}/2 = 24.6$ cm. On the lower left are the E-lines for the TM_{02} mode, on the lower right those of the TM_{03} mode. These have additional closed loops in the vertical direction with associated E_y-components and a wider spacing between successive maxima in the horizontal direction. Thus, for the TM_{02} mode, the maxima occur at intervals of $\lambda_{g2}/2 = 26.8$ cm, for the TM_{03} mode at intervals of $\lambda_{g3}/2 = 32.1$ cm. Axial distributions of the four modes are shown in Figure 12 with an assumed standing-wave ratio of 1.36 for each. Note that for the TEM mode at the bottom, there are four half-wavelengths in

31
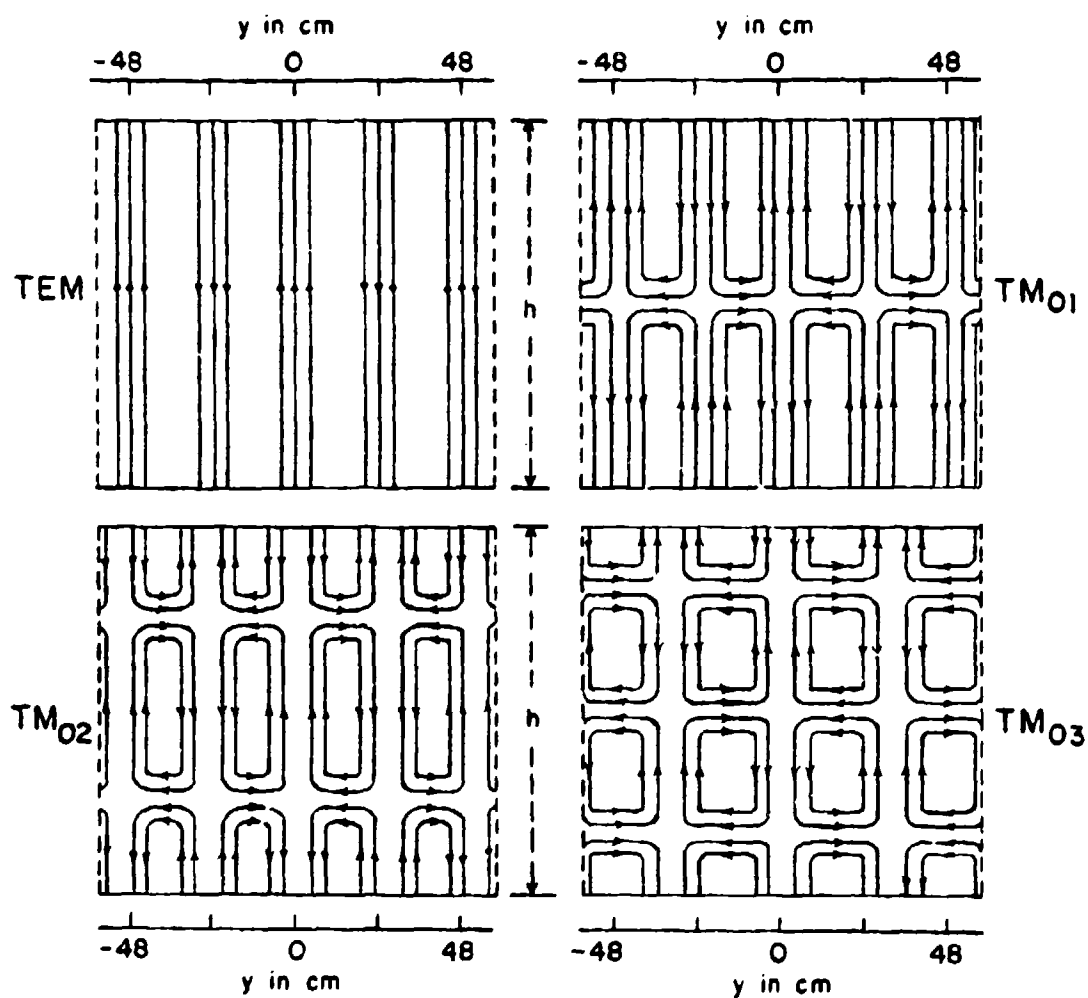
Fig. 11   Electric field lines for four parallel-plate modes in working volume
$\lambda = 48$ cm.
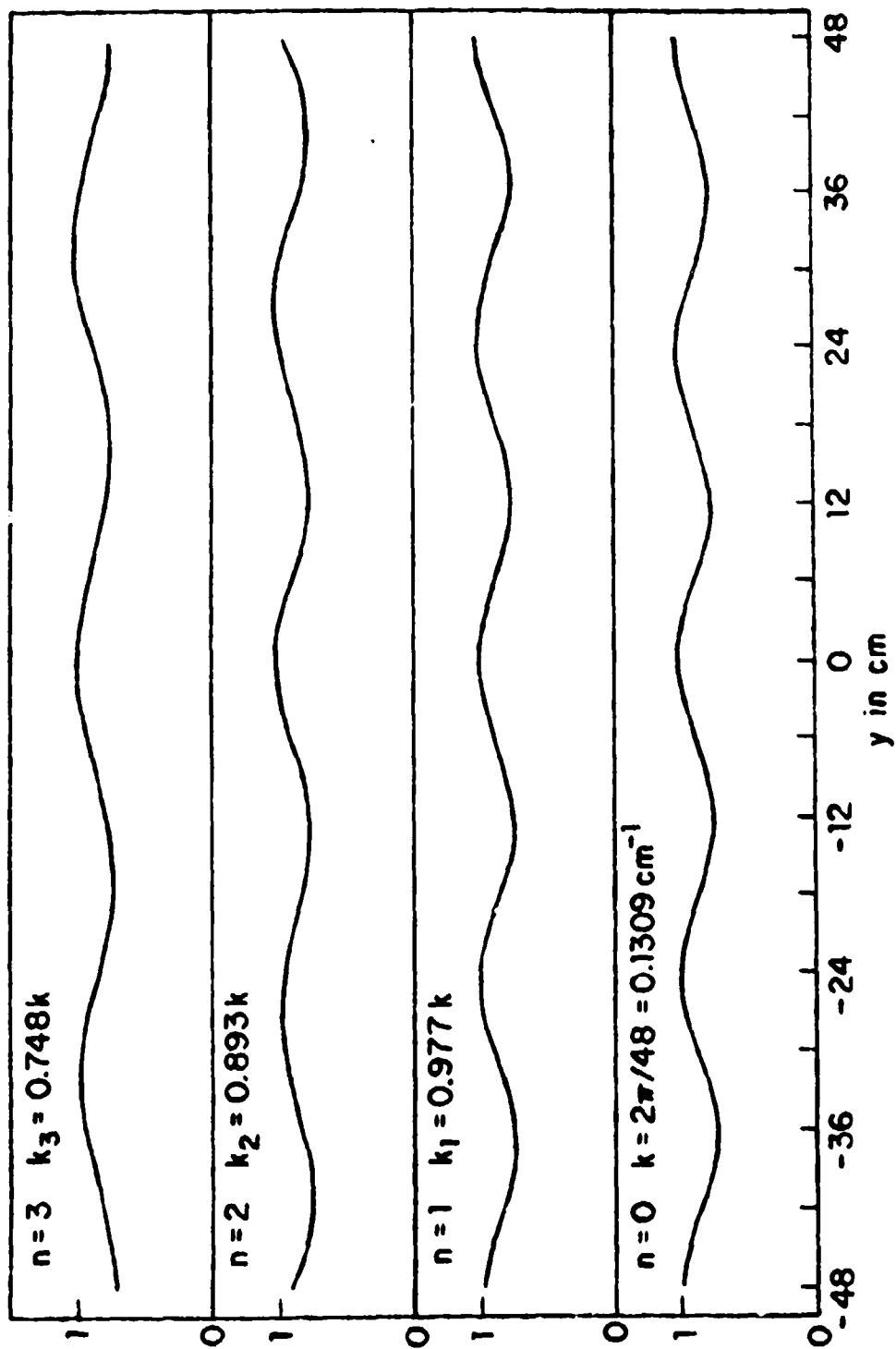
Fig. 12   Distribution of standing waves in working volume for each mode; SWR = 1.36
λ = 48 cm

33

the range $-48 \text{ cm} \leq y \leq 48 \text{ cm}$, whereas for the TM_{03} mode at the top, there are only three half-wavelengths in the same range.

When $h = 75 \text{ cm}$ and $f = 264 \text{ MHz}$ or $\lambda = 113.6 \text{ cm}$, the only propagating TM modes are the TEM mode and the TM_{01} mode. For the latter, the cut-off wavelength is $\lambda_{c1} = 2h = 150 \text{ cm}$, and the guide wavelength is $\lambda_{g1} = 174 \text{ cm}$. The formulas (1) - (3) apply with $n = 0$ for the TEM mode and $n = 1$ for the TM_{01} mode.

SECTION VI

THE MEASURED FIELD IN THE WORKING VOLUME: h = 2.25λ = 108 cm, f = 626.5 MHz

The principal components, E_z and E_y, of the electric field in the
working volume were measured as functions of the longitudinal variable y
with the transverse variables x and z as the parameters. Consider first the
field with f = 626.5 MHz when h = 108 cm = 2.25λ and λ = 48 cm. (The field
with h = 75 cm = 0.66λ with λ = 113.6 cm is studied in the next section.)

In Figure 13 are shown measured distributions of $|E_z|$ and $|E_y|$ in the
yz-plane at x = 1.7 cm, i.e., very near the central plane x = 0 of the
parallel-plate region. The parameter z/h ranges from 0 at the bottom to
z/h = 1 at the top. The field along the ground plane z/h = 0 was measured
with the monopole probe mounted on the movable metal disk; the field along
the underside of the top plate was measured with the monopole probe that
moves in longitudinal slots. The field at all other values of z/h was
measured with the movable dipole space probe that is supported by a long
tube parallel to the x-axis that moves laterally and vertically. The
component E_z was measured with the dipole in the vertical position, the
component E_y with the dipole in the horizontal position. Only the magni-
tudes $|E_z|$ and $|E_y|$ are shown in Figure 13. Actually, both magnitude and
phase were measured. Furthermore, for each height z/h shown in Figure 13
except z/h = 0, the fields were measured at seven values of x covering one-
half of the working volume.

Selected graphs at z/h = 0.08, 0.45, and 0.91 as measured with the
space probe and at z/h = 1 as measured by the monopole probe protruding from
the top plate are shown in Figures 14 through 17 for E_z and in Figures 18
through 20 for E_y. Of particular interest are the four graphs of $|E_z|$ shown
in Figure 21. They reveal the striking change in the standing-wave pattern
in the plane x = 1.7 cm from near the top (z/h = 0.91) to near the bottom
(z/h = 0.079). Clearly there are three standing-wave maxima at the top,
four at the bottom. Actually, the standing-wave pattern for $|E_z|$ at z/h =
0.08 near the ground plane and shown at the bottom in Figure 21 is a good
approximation of the TEM field shown at the bottom in Figure 12. The
successive maxima are quite uniformly spaced at λ/2 = 24 cm and $|E_y| \doteq 0$.
On the other hand, the standing-wave pattern of $|E_z|$ at z/h = 0.91 near the
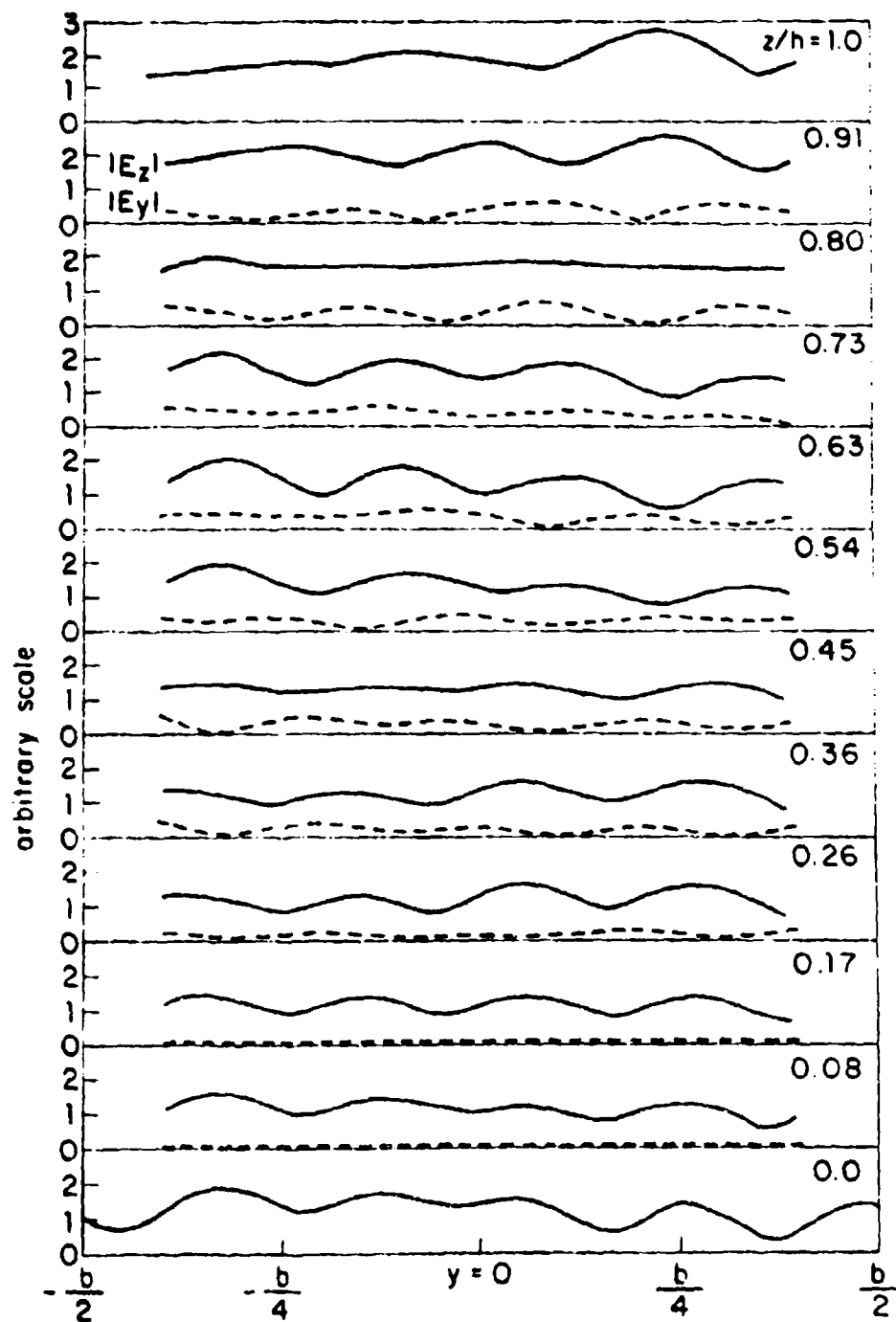
Longitudinal cross section of working volume y-z plane x = 1.7 cm
b = 115 cm = 2.4 λ ; h = 108 cm = 2.25 λ

Fig. 13   Measured magnitude of the vertical and longitudinal
components of the electric field in the working volume

Fig. 14 Measured magnitude and phase of E_z in working volume of model simulator.

Fig. 15 Measured magnitude and phase of E_z in working volume of model simulator

Fig. 16 Measured magnitude and phase of E_z in the working volume of model simulator

Fig. 17 Measured magnitude and phase of E_z on parallel plate of model simulator

Fig. 18 Measured magnitude and phase of E_y in
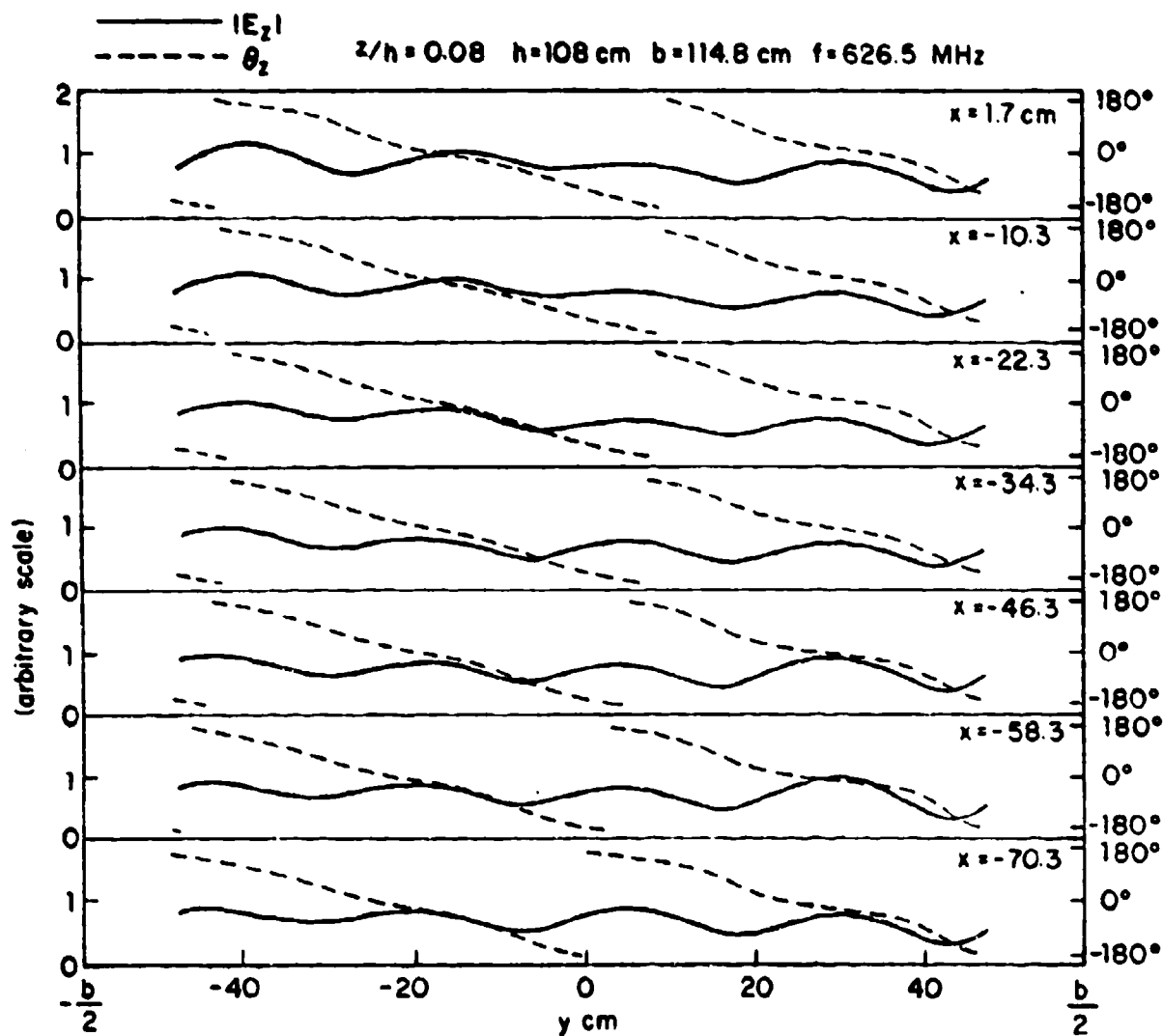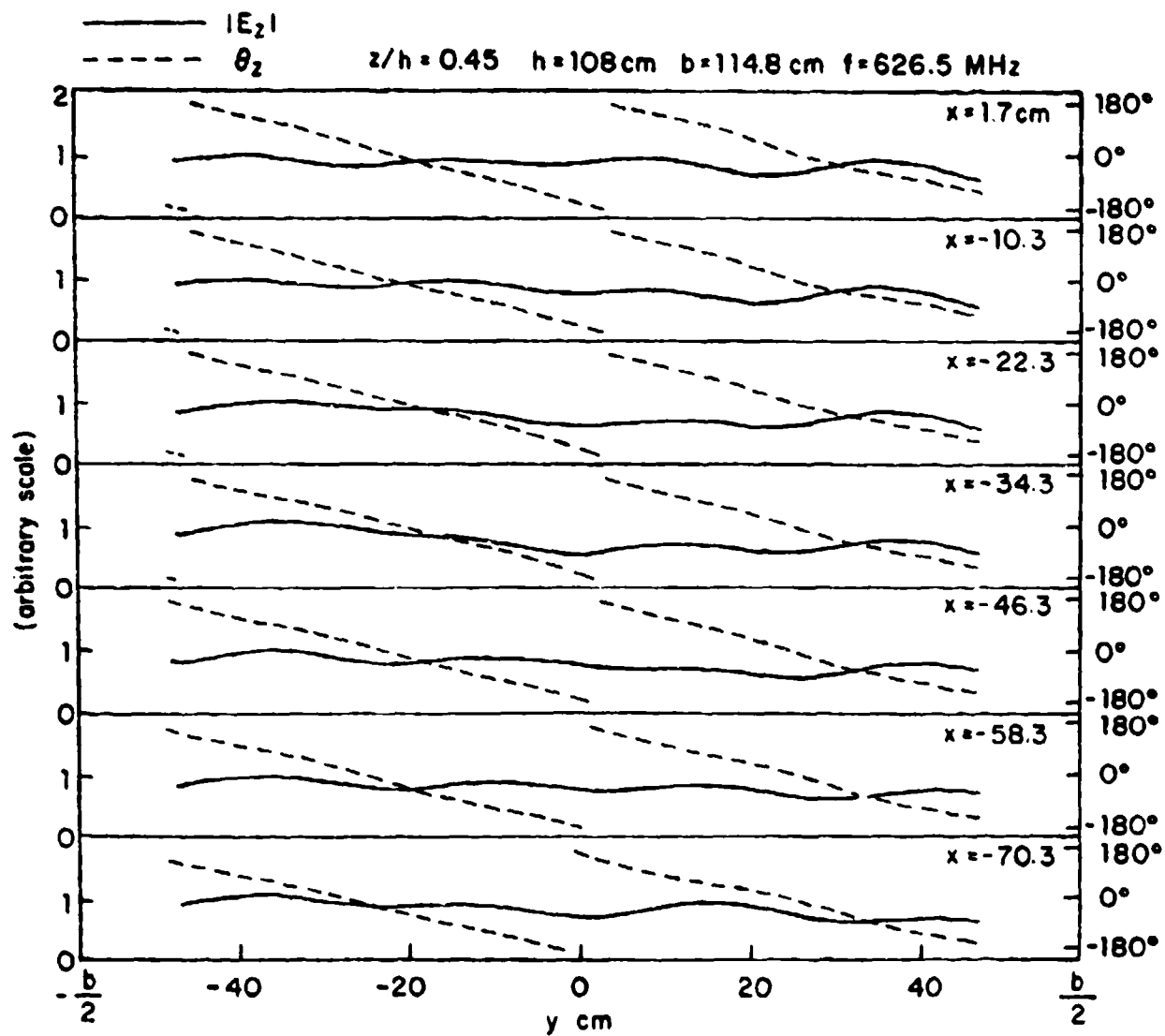working volume of model simulator.

Fig. 19 Measured magnitude and phase of E_y in working volume of model simulator.

Fig. 20 Measured magnitude and phase of E_y in
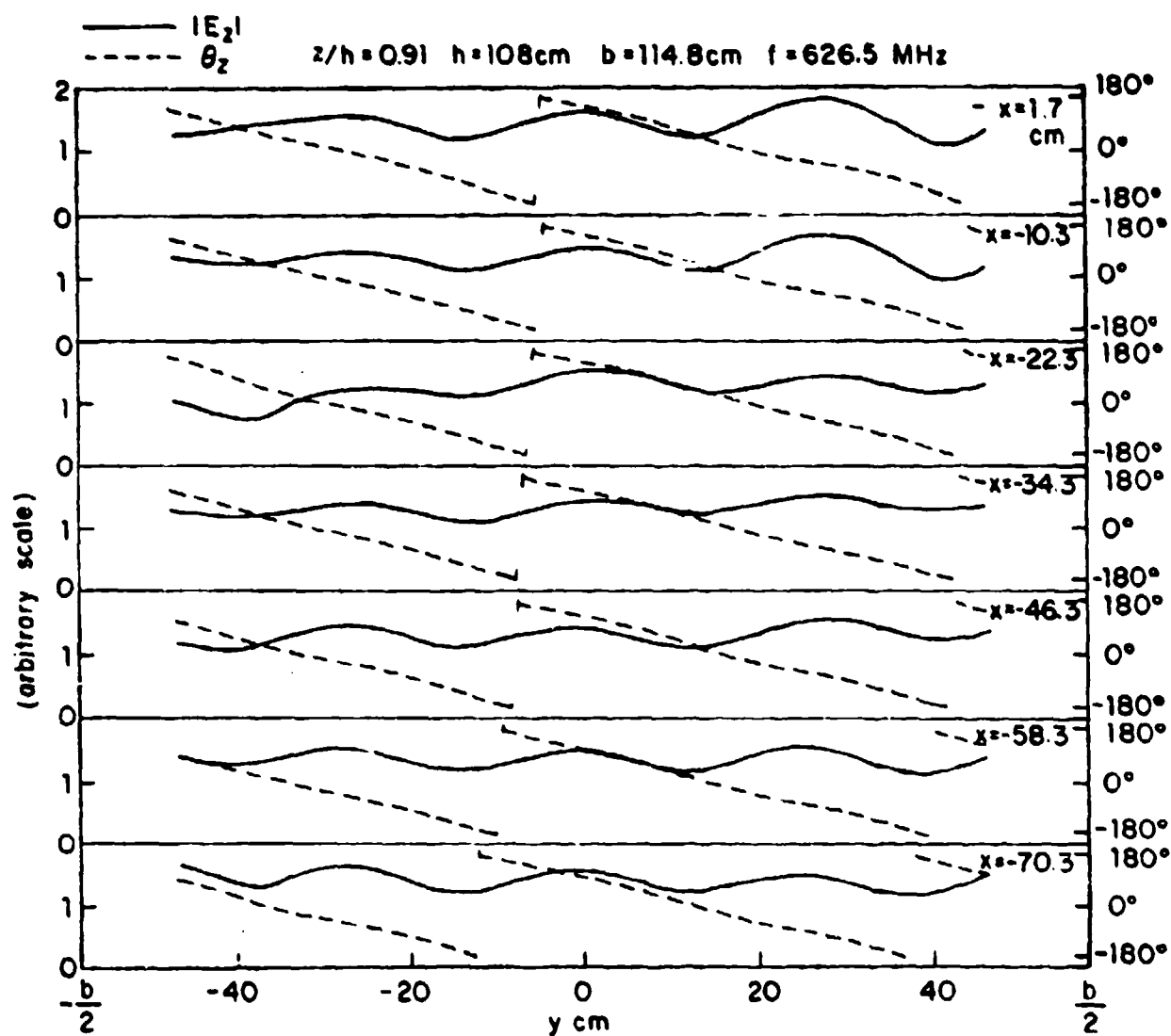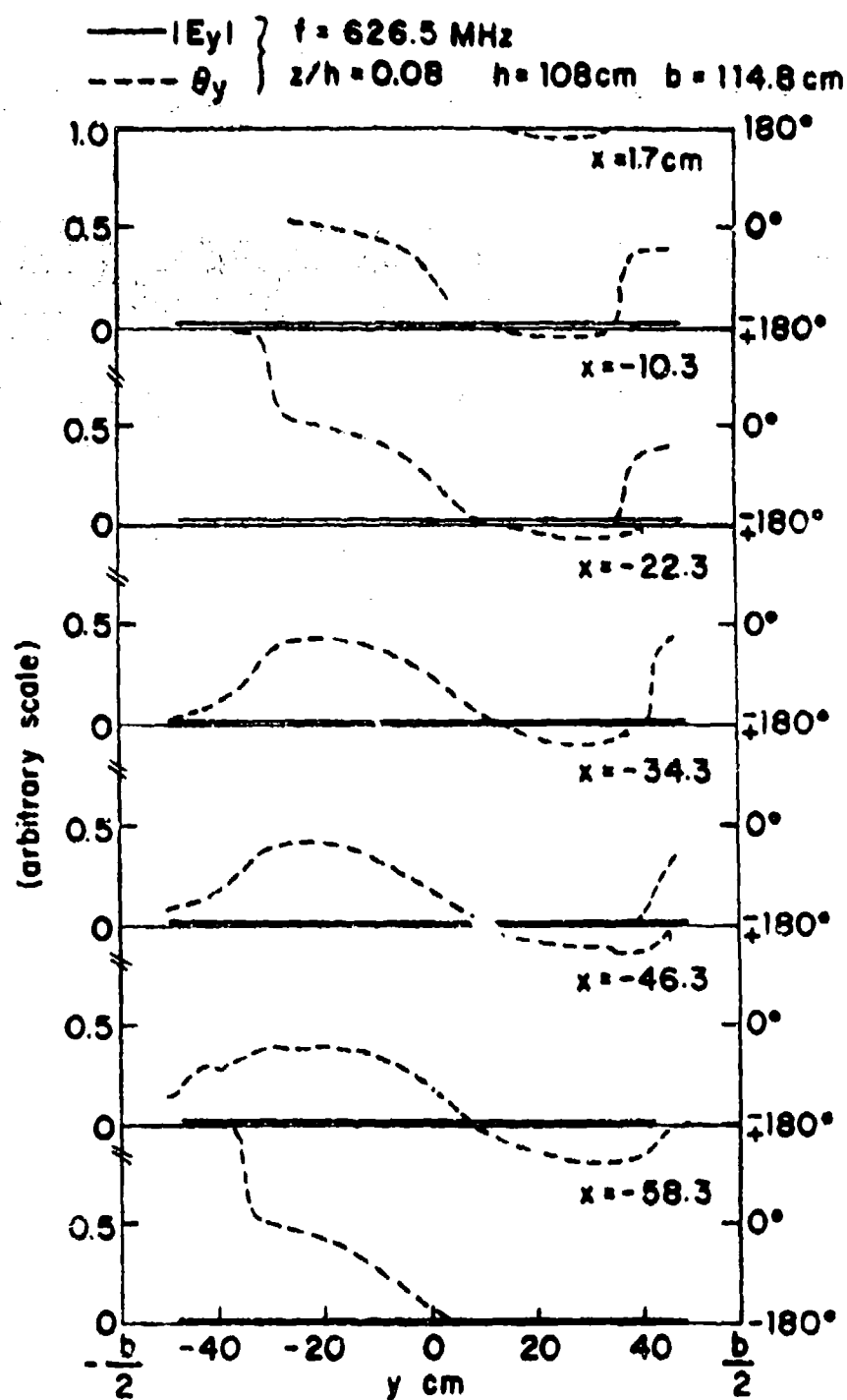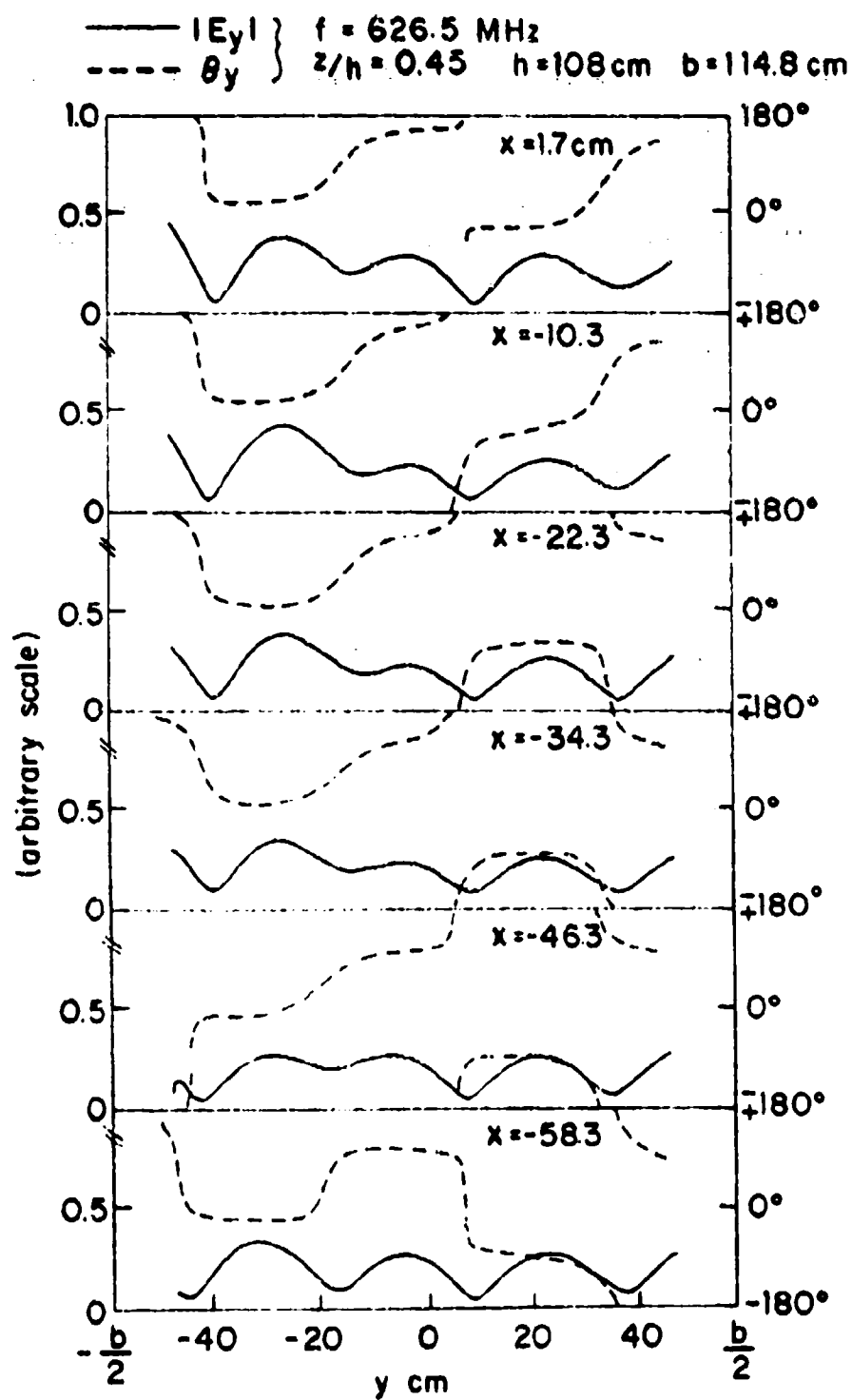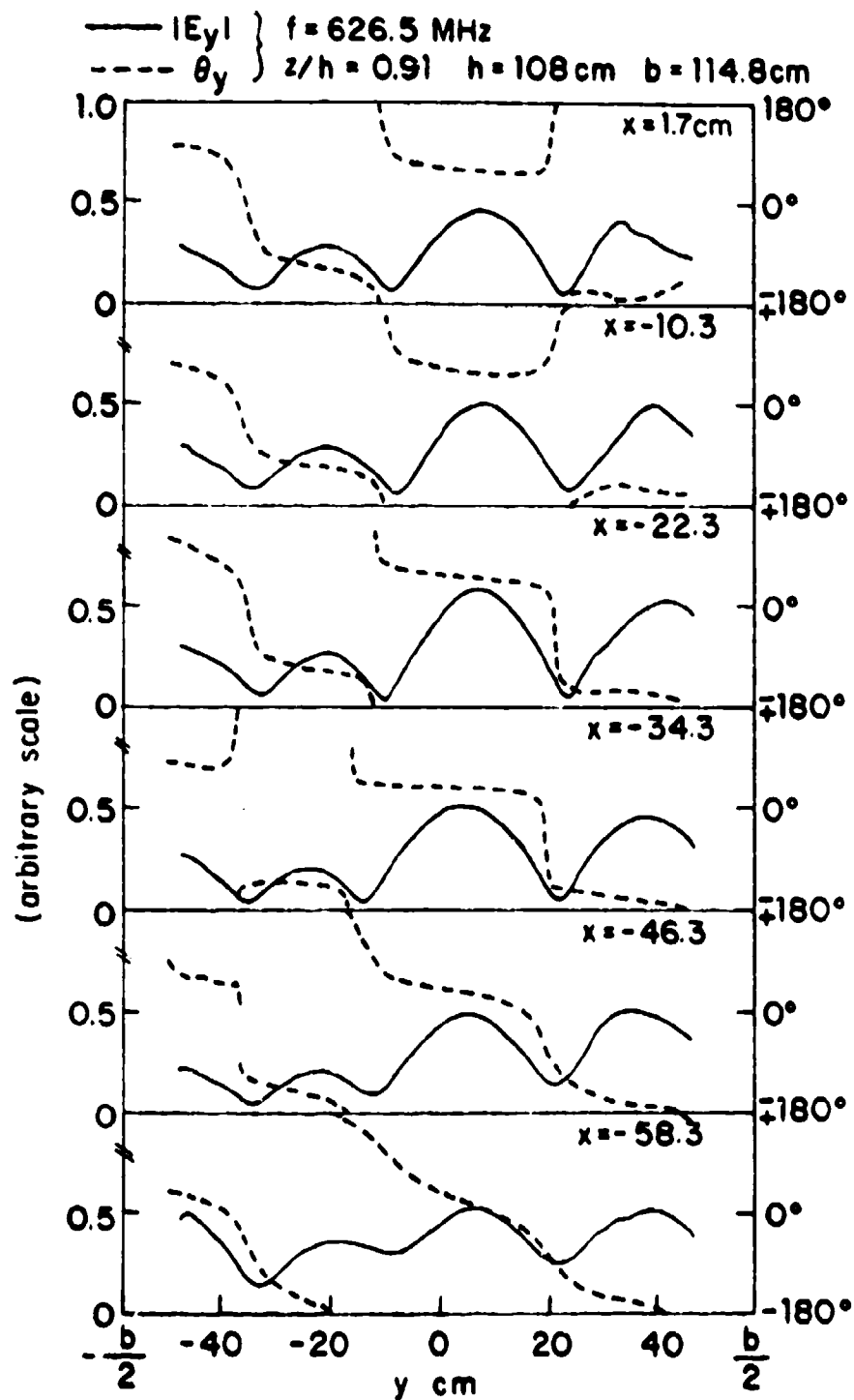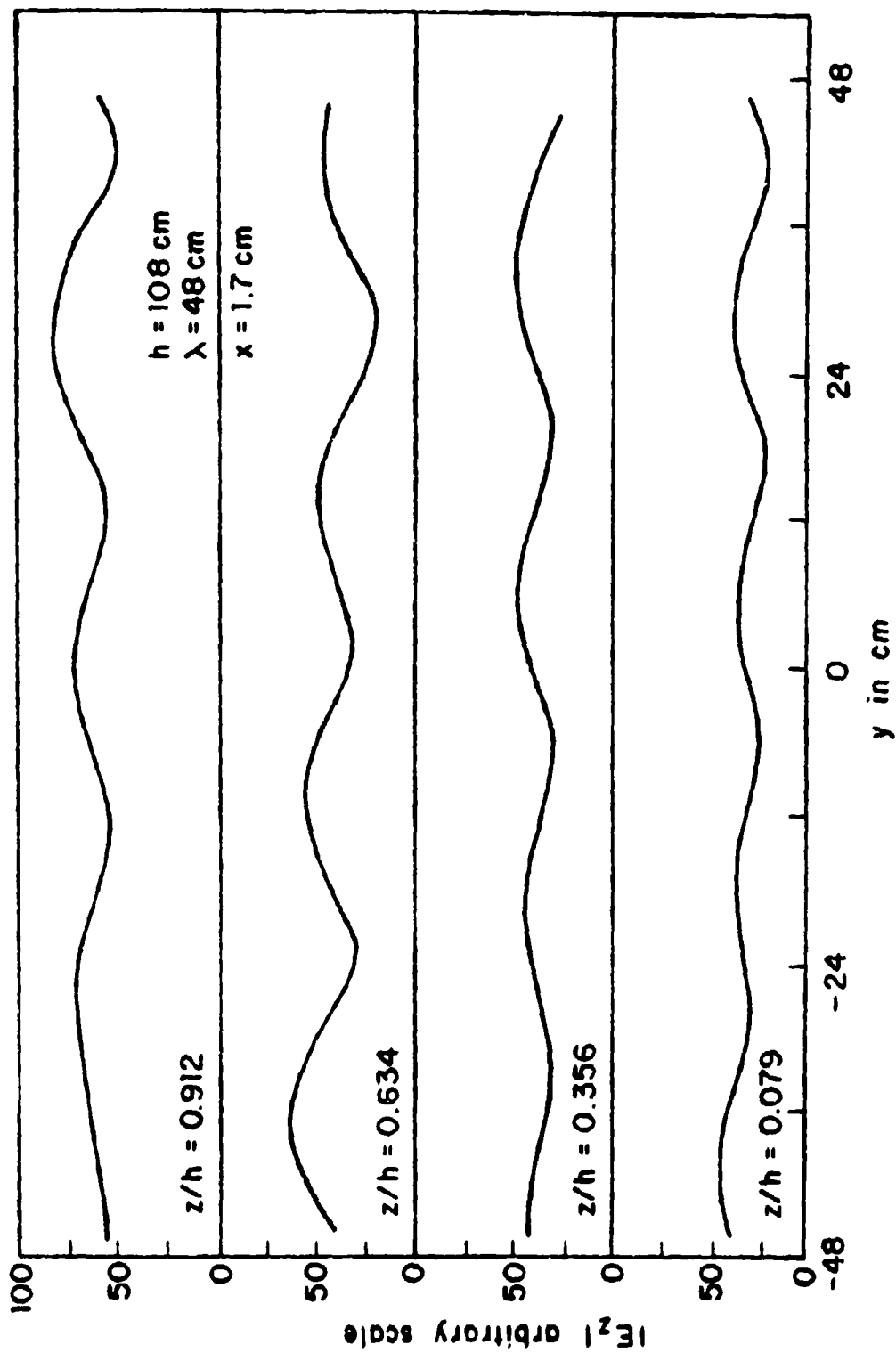working volume of model simulator

Fig. 21 Measured $|E_z|$ near center ($x = 1.7$ cm) of working volume at four heights

h = 108 cm
λ = 48 cm

x = 1.7 cm

z/h = 0.912

z/h = 0.634

z/h = 0.356

z/h = 0.079

y in cm

$|E_z|$ arbitrary scale

top plate is quite different in that there are more nearly three instead of four standing half-wavelengths in the distance -48 cm $\leq$ y $\leq$ 48 cm. This is shown at the top in Figure 21. Thus, the measured graph at the top in Figure 21 resembles the graph at the top in Figure 12 for the standing-wave distribution of the n = 3 mode in the parallel-plate region. It is also evident from Figure 13 and Figures 18 through 20 that E_y is significant. It has a standing-wave distribution with a wavelength near λ_{g3} and is displaced from that of $|E_z|$ by nearly $\lambda_{g3}/4$.

In order to interpret the extensive data contained in the measured field in the working volume, the graphs shown in Figure 22 were constructed from the measured data. They show the measured $|E_z|$ as a function of the vertical coordinate z at seven different transverse positions x across the central plane (y = 0) of approximately one-half of the working volume. The distributions are seen to be quite comparable in magnitude and shape, thus indicating a field that is reasonably independent of the transverse coordinate x, as is implicit for the ideal TEM and TM_{0n} components. The fact that E_z is approximately independent of x also indicates that the contribution to $|E_z|$ by possible $TE_{0\ell}$ modes is small. This is considered in a later section.

At each cross section (y = constant), E_z can be approximated by a super-position of the TEM and the three propagating TM_{0n} modes. The relative amplitudes of these modes cannot be determined theoretically, but can be obtained from the measured distribution of $E_z = E_{zR} + iE_{zI}$. Thus,

$$E_z(y) = A(y) + B(y)\cos(\pi z/h) + C(y)\cos(2\pi z/h) + D(y)\cos(3\pi z/h) \qquad (14)$$

where $A(y) = A_R(y) + iA_I(y)$ is the complex amplitude of the TEM mode, $B(y) = B_R(y) + iB_I(y)$, $C(y) = C_R(y) + iC_I(y)$, and $D(y) = D_R(y) + iD_I(y)$ are, respectively, the complex amplitudes of the TM_{0n} modes, n = 1, 2, 3. The real amplitudes $A_R(y)$, $B_R(y)$, ..., $A_I(y)$, $B_I(y)$, ..., can be determined by fitting the distribution (14) to the corresponding measured curve at each cross section y = constant. Since E_z is approximately independent of x, it is sufficient to evaluate the amplitude coefficients at x = 0. The appropriate values are shown in Table 1 with all phases referred to the origin of coordinates x = y = z = 0. Graphs of the coefficients as functions of y are shown in Figure 23. It is seen that they form standing-wave patterns with

45
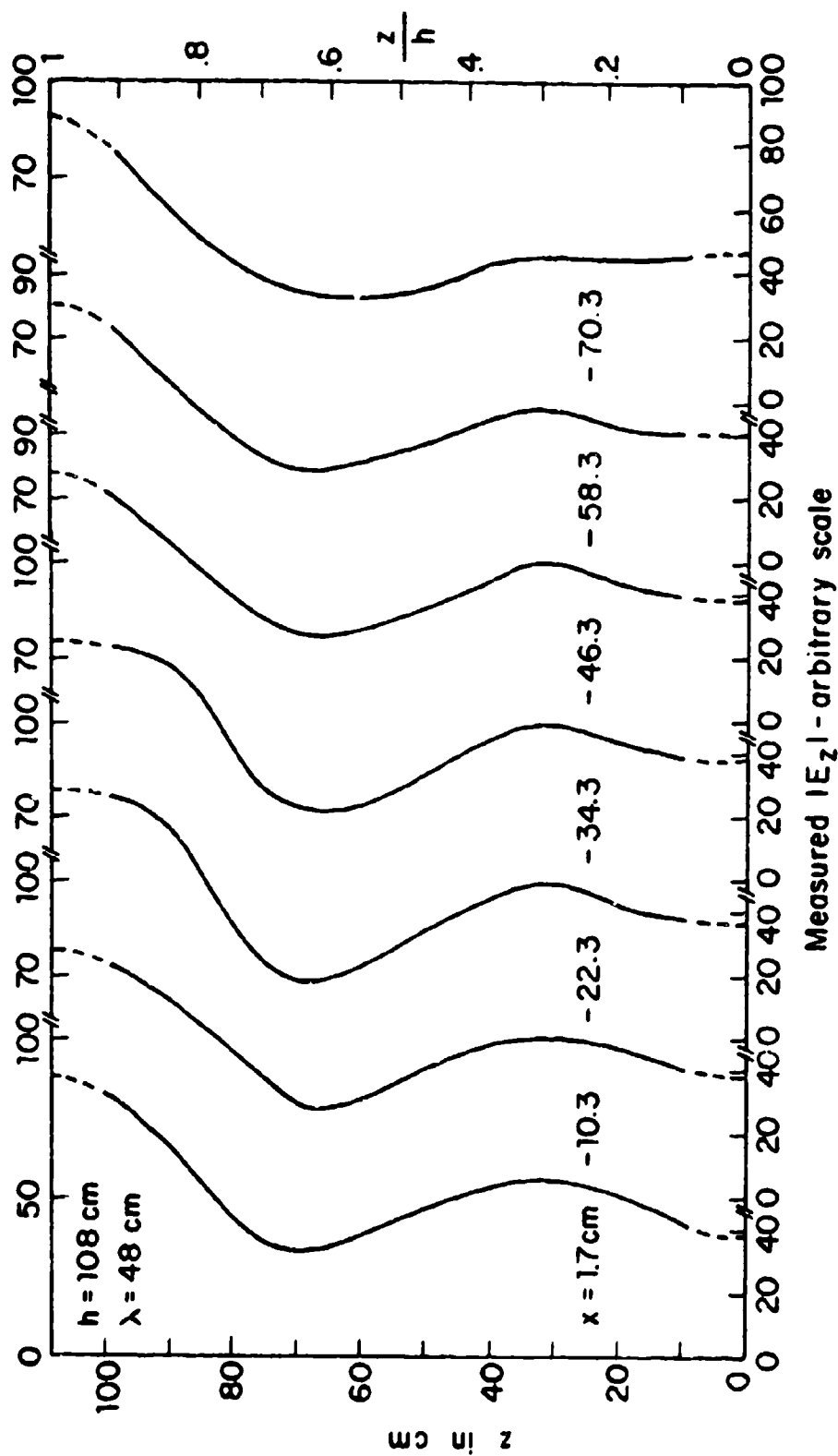
Fig. 22 Measured electric field near central plane (y=0) in working volume

TABLE 1

COEFFICIENTS REFERRED TO y = 0, z = 0, OBTAINED FROM MEASURED DATA

y(cm) =	0	-6	-12	-18	-24	-30	-36	-42	-46.5
$A_I(y)$	-41.2	-10.0	25.9	43	35	4.4	-34.7	-44	-40.2
$B_I(y)$	26.2	40.3	24.5	-0.2	-30	-37.3	-23.6	-1.5	19.6
$C_I(y)$	-3.5	-7.9	-5.1	-4	10.1	12.8	15.6	2.1	-6.4
$D_I(y)$	18.6	14.2	6.7	1.9	-9.0	-12.7	-15.3	-3.7	-3.2
$A_R(y)$	25.0	39.5	34.2	13.4	-19.8	-42.0	-33.4	-10.4	8.9
$B_R(y)$	16.7	-11.9	-35.3	-43.7	-18.8	16.4	45.5	46	23.1
$C_R(y)$	-2.1	-10.0	-4.7	2.7	2.5	7.0	-0.7	-4.8	-4.3
$D_R(y)$	1.0	7.6	5.8	4.1	1.6	-4.3	-6.2	-8.9	-6.9
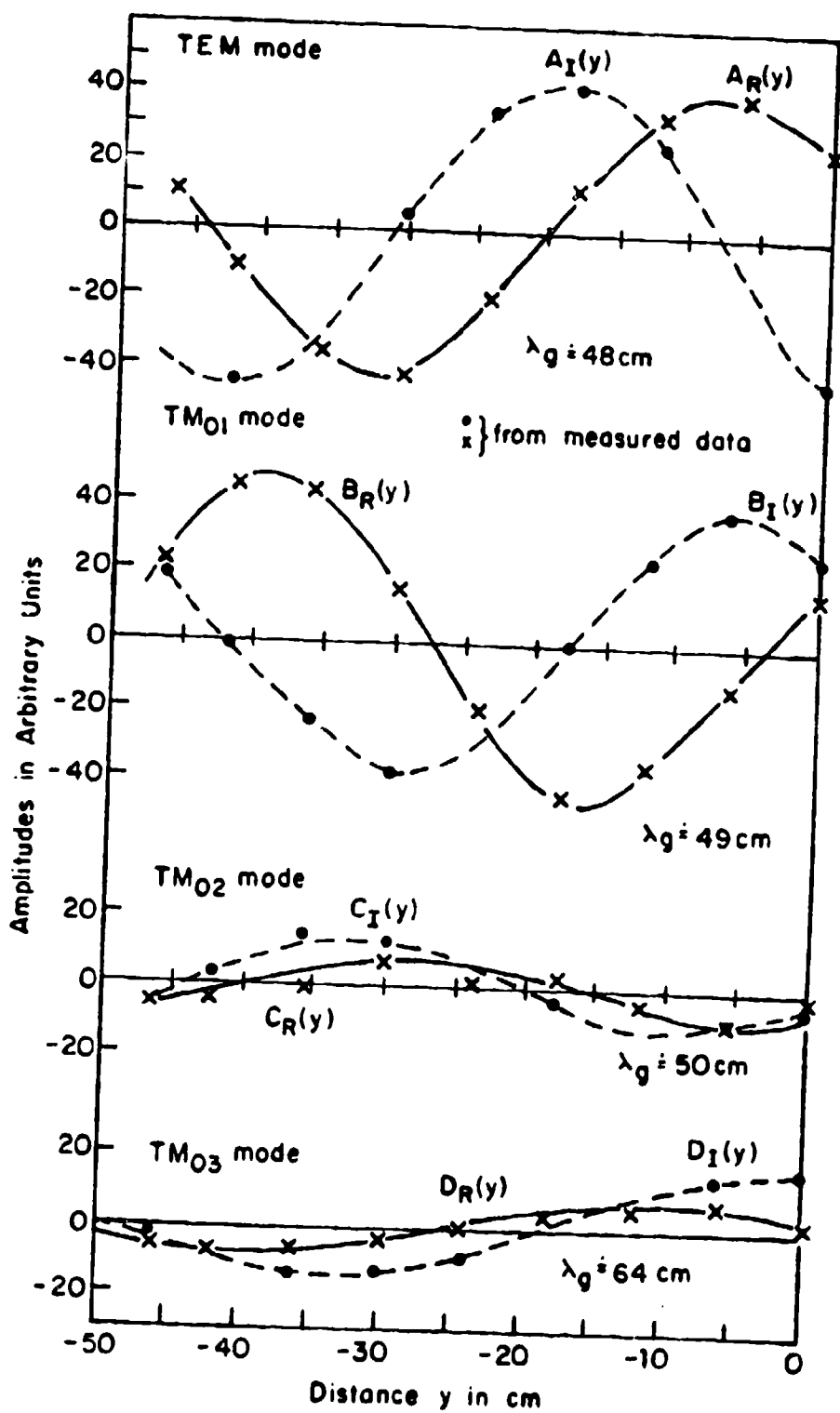
Fig. 23 Amplitudes of TEM and TM_{On} modes in forward half
of working volume

the wavelength $\lambda = 48$ cm for the A coefficients, $\lambda_{g1} = 49.1$ cm for the B coefficients, $\lambda_{g2} = 50$ cm for the C coefficients, and $\lambda_{g3} = 64$ for the D coefficients. These wavelengths are in good agreement with the ideal wavelengths, $\lambda = 48$ cm for the TEM mode, and $\lambda_{g1} = 49.2$ cm, $\lambda_{g2} = 53.7$ cm, and $\lambda_{g3} = 64.2$ cm for the TM_{0n} modes with $n = 1, 2, 3$.

When the coefficients in Table 1 are substituted in equation (14), E_z can be calculated as a function of z at any desired cross section. In Figures 24a and 24b are shown in broken lines the calculated vertical distributions of the real and imaginary parts of E_z at the center ($x = 0$, $y = 0$) of the working volume, and at $x = 0$ and successively $y = -6, -12, -18, -24, -30, -36,$ and -42 cm toward the generator. Also shown in solid lines are the corresponding measured distributions. It is evident that the assumed approximate representation of the field as a superposition of the ideal parallel-plate TEM and TM_{0n} modes is a good one throughout the working volume of the model simulator. It is also evident that the total E_z differs greatly from the part contributed by the TEM mode alone, which is constant in z. Figure 23 shows that the amplitudes of the TEM and TM_{01} modes are almost the same. Their standing-wave distributions and phases are such that $|E_z|$ is substantially greater near the top plate, $z = h$, than near the ground plane, $z = 0$.
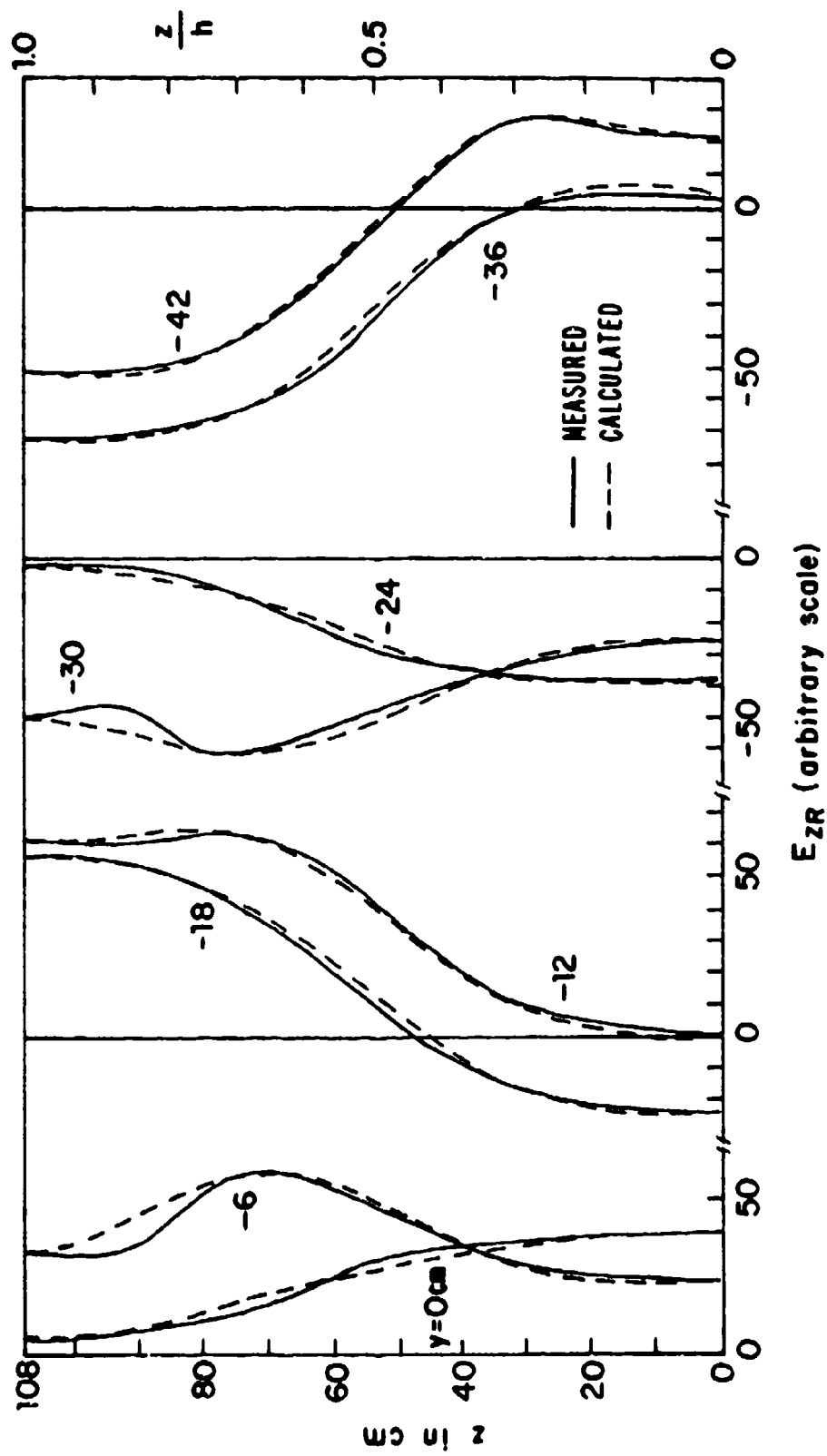
Fig. 24a Real part of vertical electric field in working volume. (Phase reference: x = y = z = 0)
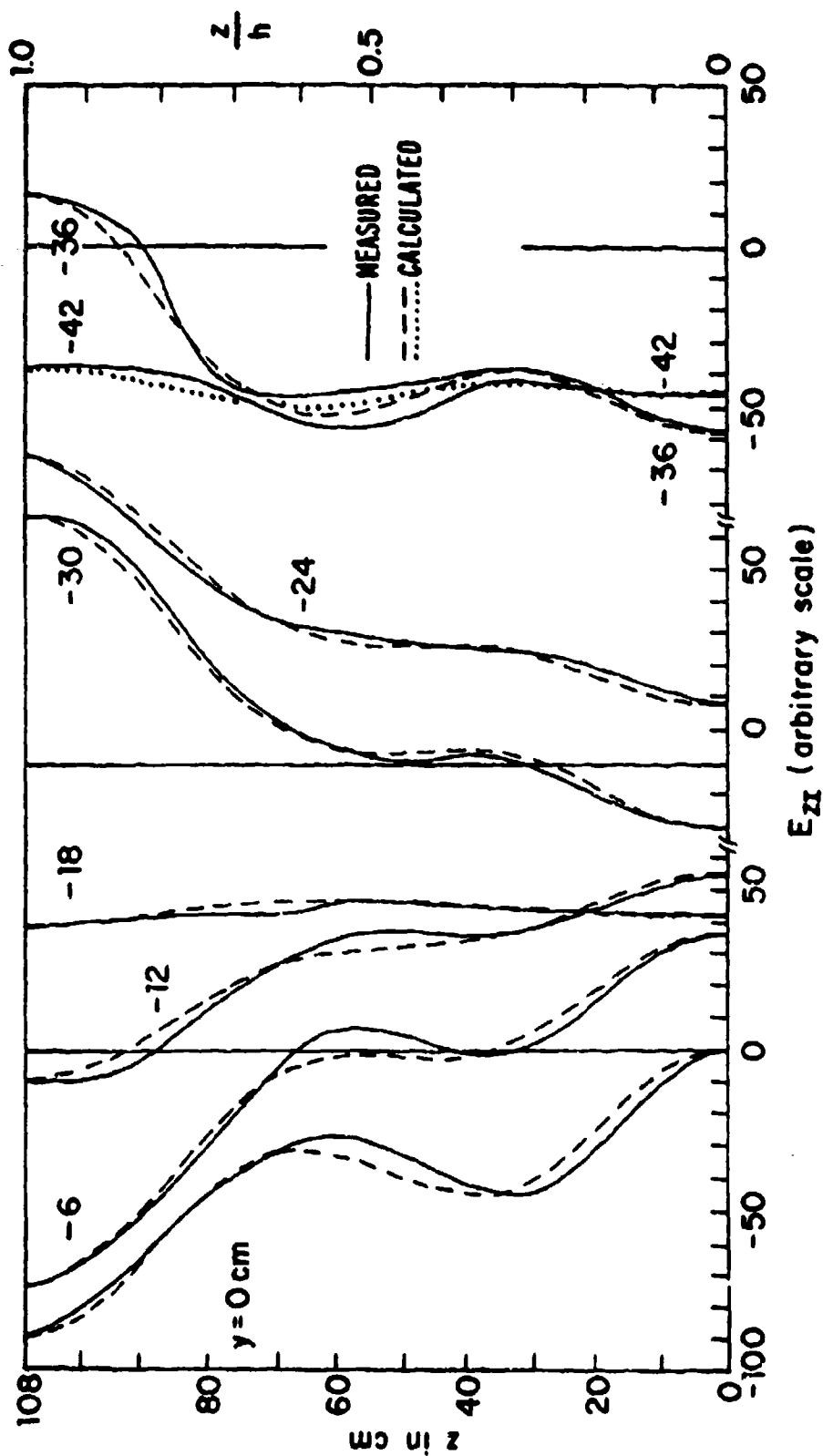
Fig. 24b Imaginary part of vertical electric field in working volume. (Phase reference: $x = y = z = 0$)

51

SECTION VII

THE MEASURED FIELD IN THE WORKING VOLUME: $h = 0.66\lambda = 75$ cm, $f = 264$ MHz

The components E_z and E_y in the working volume and adjacent regions were also measured with $f = 264$ MHz when $h = 75$ cm $= 0.66\lambda$ and $\lambda = 113.6$ cm. To simplify the presentation of the data, these components of the field were measured as functions of z/h with $y = 0$ and x as parameter. The measured graphs of $|E_z|$, $|E_y|$, θ_z, and θ_y are shown in Figure 25 for eight values of x. From them, the real and imaginary parts of E_z were determined, as shown in Figure 26.

Corresponding to equation (14), the vertical electric field is approximated by:

$$E_z(y) = A(y) + B(y)\cos(\pi z/h) \tag{15}$$

It follows that

$$A_R(y) + iA_I(y) = E_{zR}(y) + iE_{zI}(y), \quad \text{at } z = h/2 \tag{16}$$

Graphs of $A_R(y)$ and $A_I(y)$ as obtained from Figure 25 as functions of y are shown in the upper half of Figure 27. The half-wavelength is quite accurately $\lambda/2 = 56.8$ cm as determined from the graph of the large real part $A_R(y)$. Graphs of the amplitudes $B_R(y)$ and $B_I(y)$ of the part of $E_z(y)$ due to the TM_{01} mode are near the center of Figure 27; the associated graphs of the real and imaginary parts of $E_y(y)$, which is entirely TM_{01}, are at the bottom. Here the wavelength $\lambda_{g1} = 174$ cm is also confirmed by the standing-wave patterns of the imaginary parts. As with the higher frequency and greater height h of the working volume, the approximate representation of E_z and E_y by TEM and TM_{0n} modes is quite satisfactory.

FIG. 25   MEASURED ELECTRIC FIELD IN TRANSVERSE PLANE y = 0
OF WORKING VOLUME; b = 114.8 cm, 2a = 175 cm, h = 75 cm,
f = 264 MHz.

Fig. 26 Real and Imaginary Parts of E_z in Working Volume and Adjacent Regions; Phase Referred to $x = y = z = 0$.

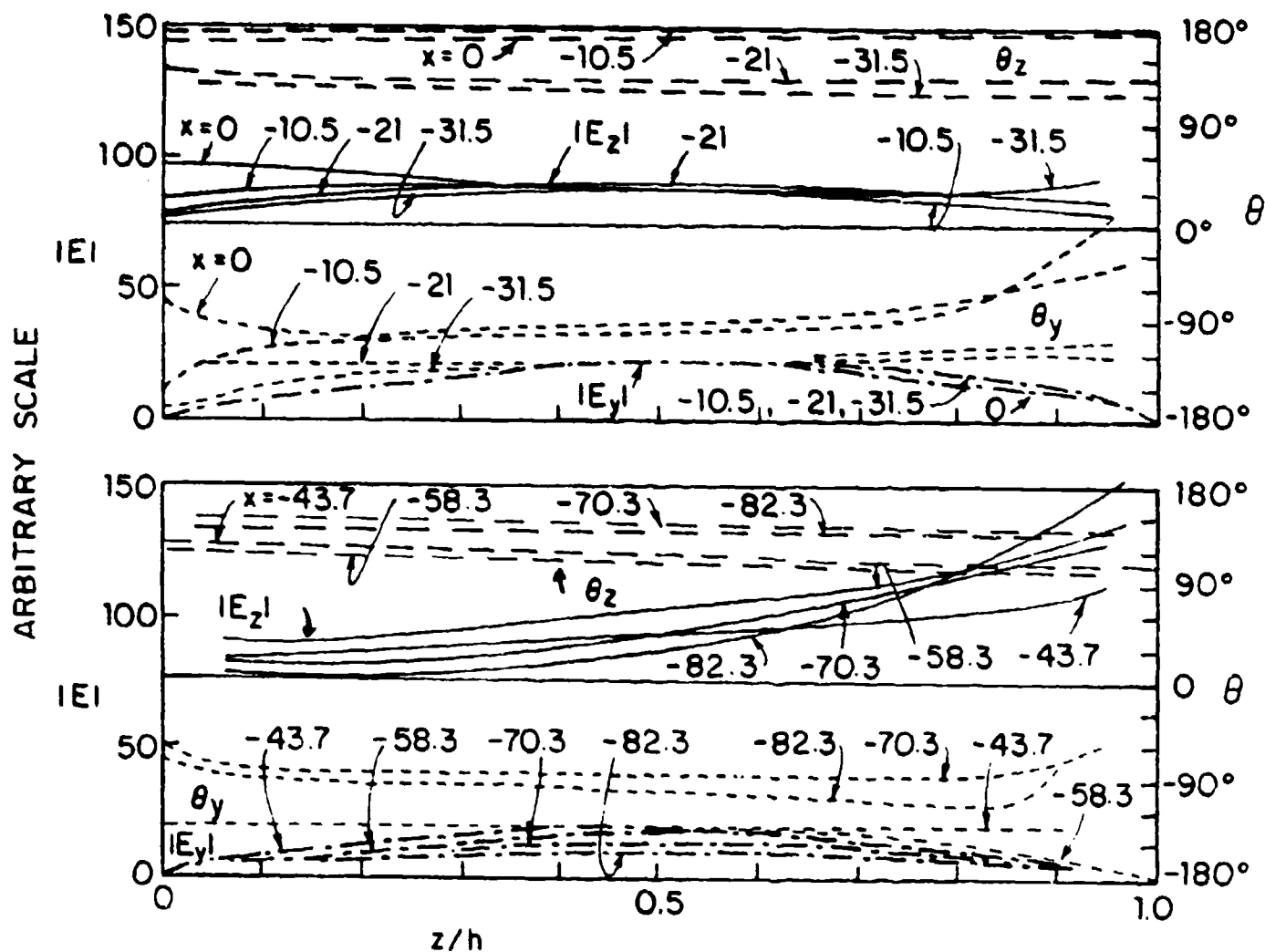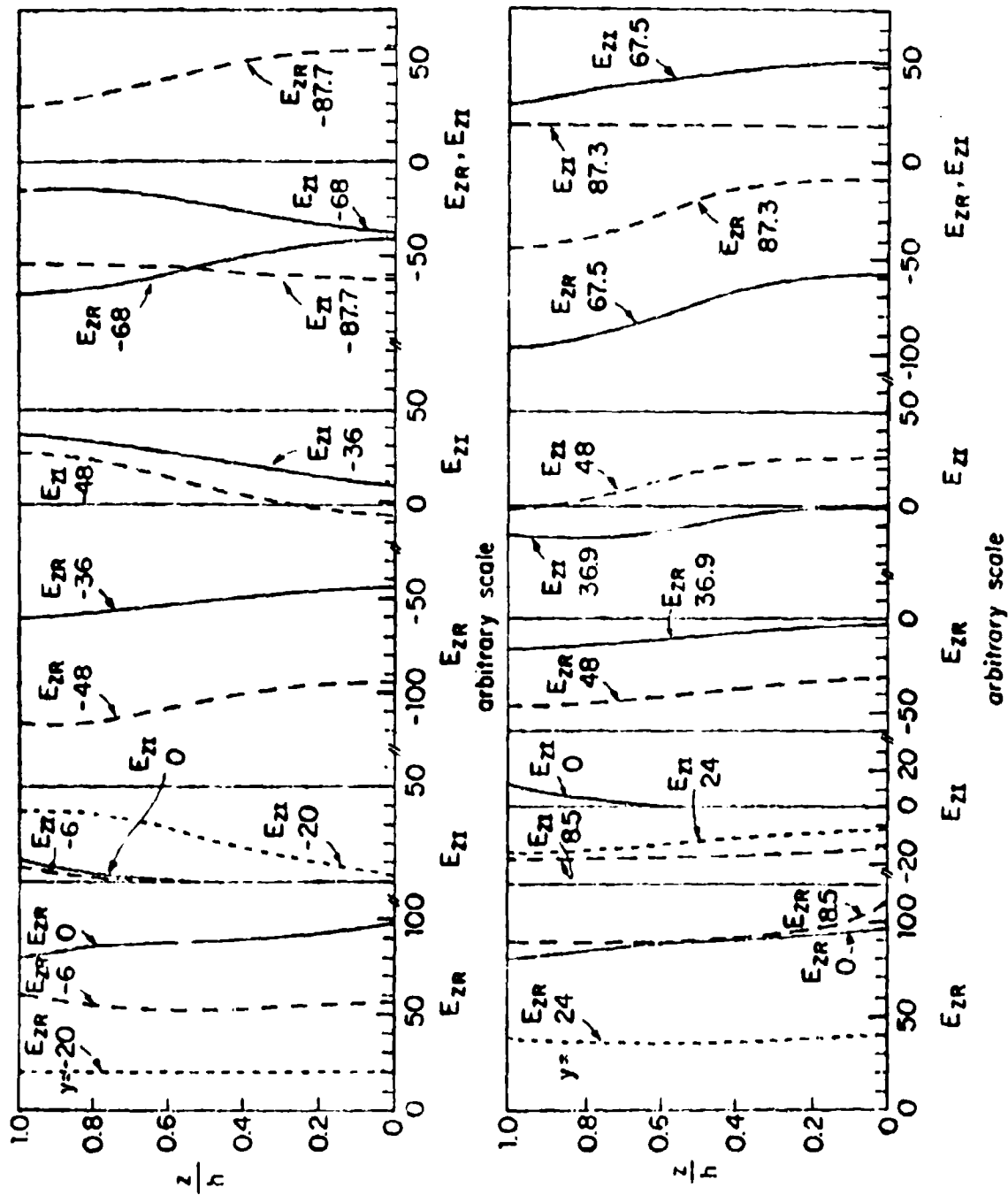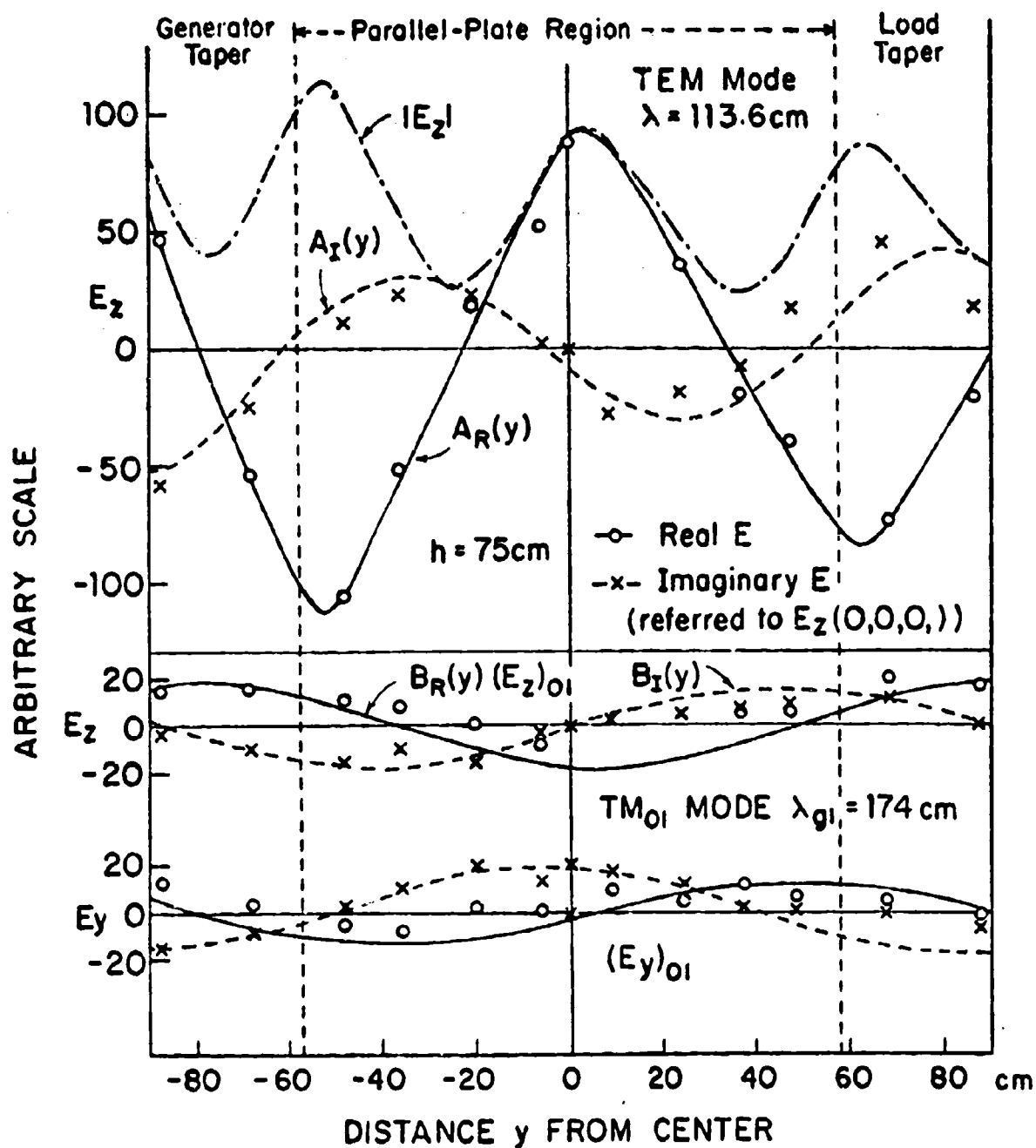FIG. 27 GRAPHS OF THE REAL AND IMAGINARY PARTS OF $E_z(y) = A(y) + B(y)\cos(\pi z/h)$ AND $E_y(y)$ AS FUNCTIONS OF y IN AND NEAR THE PARALLEL PLATE REGION.

SECTION VIII

THE TRANSVERSE VARIATION OF THE ELECTRIC FIELD; TE MODES

The approximate representation of the electric field in the parallel-plate region of the simulator in terms of the TEM and TM_{0n} modes tacitly assumes that all of the components of the electromagnetic field are independent of the transverse variable x since all wave fronts are assumed to be planes perpendicular to the longitudinal y-axis. This was taken to be a good approximation because the electric field shown in Figure 22 changes relatively little as x is varied in steps from near the center of the working volume to near the edge at $x = \pm a = 87.5$ cm. It is now appropriate to examine the variation of the field with x in greater detail.

A useful starting point is the nature of the wave fronts - surfaces of constant phase - in the working volume. It is shown in conjunction with Figures 7 and 8 that the field incident on the parallel-plate region at $y = -b/2 = -57.5$ cm is essentially a traveling spherical wave. In Figures 28a, 28b, and 28c are shown the measured phase fronts of θ_z, the phase angle of E_z, in xy-planes at discrete values of z/h ranging from 1 to 0. With the measured curves are shown the phase fronts for ideal spherical traveling waves originating at the generator end of the simulator ($x = 0$, $y = -369$ cm, $z = 0$ when $h = 108$ cm). These graphs supplement those in Figures 10a and 10b which show the measured phase fronts of θ_z in yz-planes together with the phase fronts for the ideal spherical waves. It is seen from all of these diagrams that the measured phase fronts in transverse as well as in vertical planes are those of a spherical wave with superimposed oscillations due to standing waves. Clearly, the length and width of the parallel-plate region are inadequate to permit the development of plane wave fronts and the assumption that these are good approximations is acceptable only in the central part of the working volume, roughly in the range -50 cm $\leq x \leq 50$ cm, $z \leq h/2 = 54$ cm.

The measured transverse distributions of both $|E_z|$ and θ_z are shown in Figure 29 for a range of values of z from $z = 8.5$ cm $= 0.18\lambda$ near the ground plane at $z = 0$ to $z = 98.5$ cm or $h - z = 108 - 98.5$ cm $= 0.20\lambda$ from the top plate. The graphs of $|E_z|$ show a reasonably constant mean value for each value of z with a superimposed oscillation. This oscillation is a consequence

56
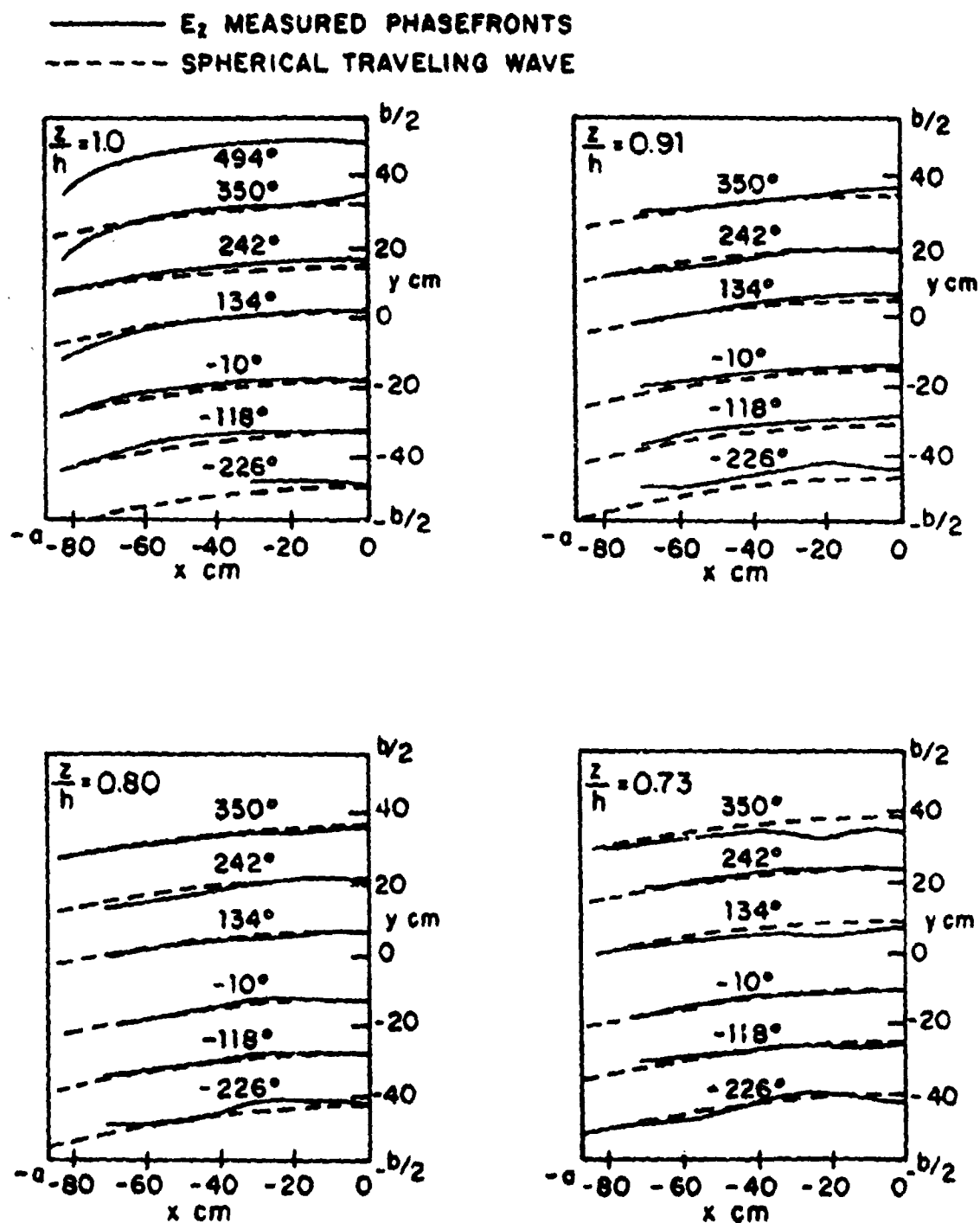
FIG. 28a MEASURED CONSTANT PHASE CURVES IN THE WORKING VOLUME;
h = 108 cm , a = 87.5 cm, b = 114.8 cm, f = 626.5 MHz.

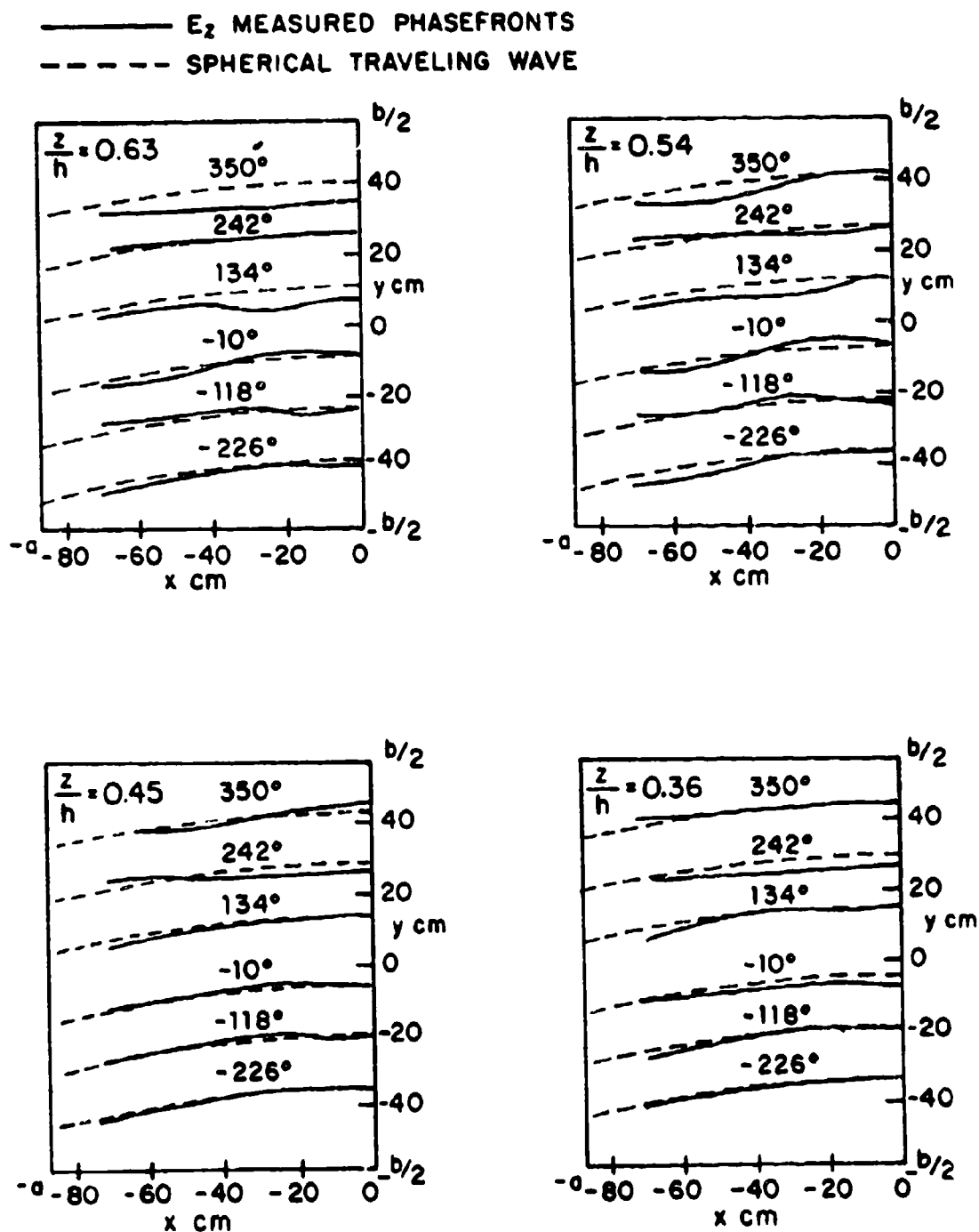FIG. 28b MEASURED CONSTANT PHASE CURVES IN WORKING VOLUME;
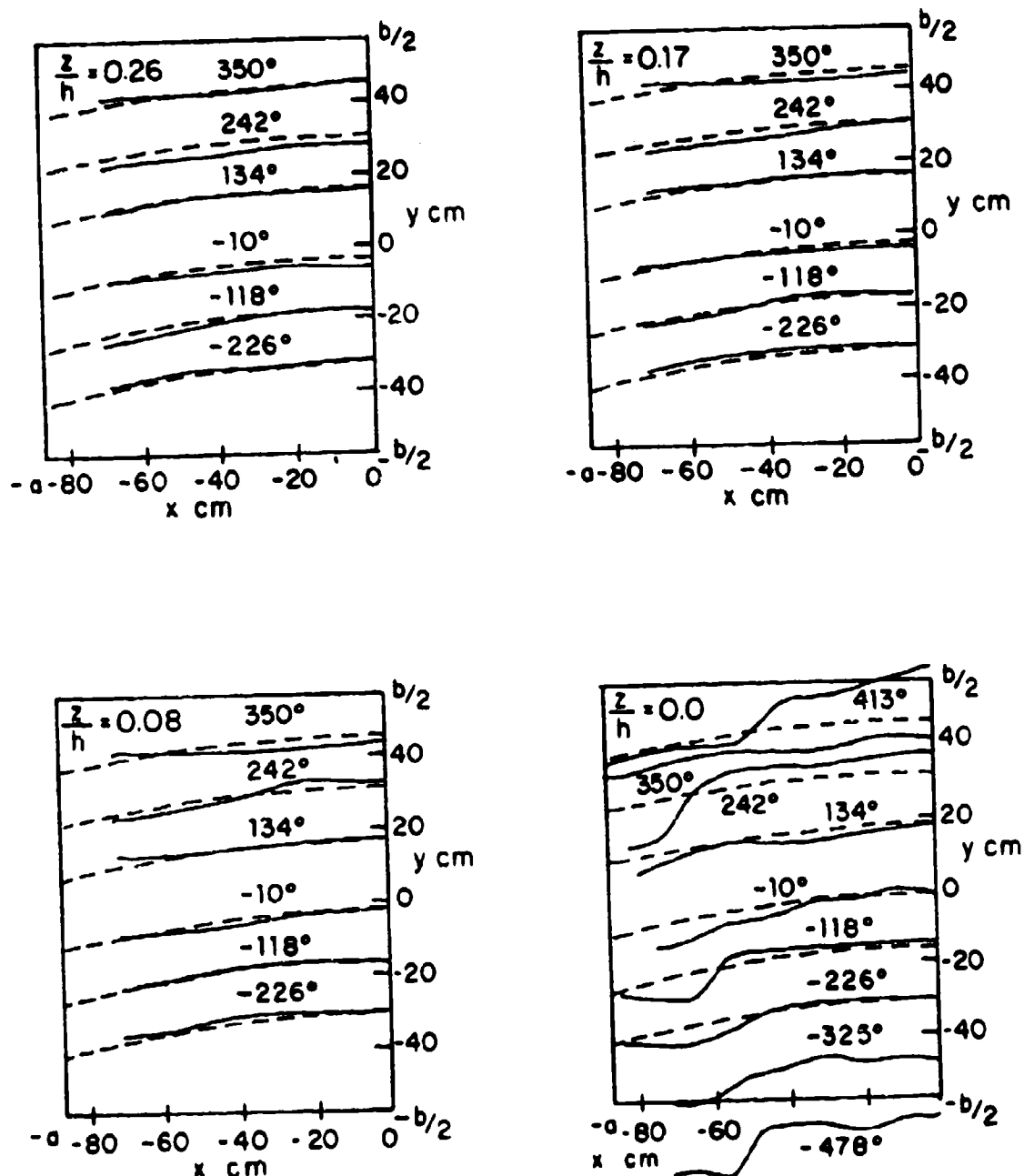h = 108 cm, a = 87.5 cm, b = 114.8 cm, f = 626.5 MHz.

FIG. 28c MEASURED CONSTANT PHASE CURVES IN WORKING VOLUME;
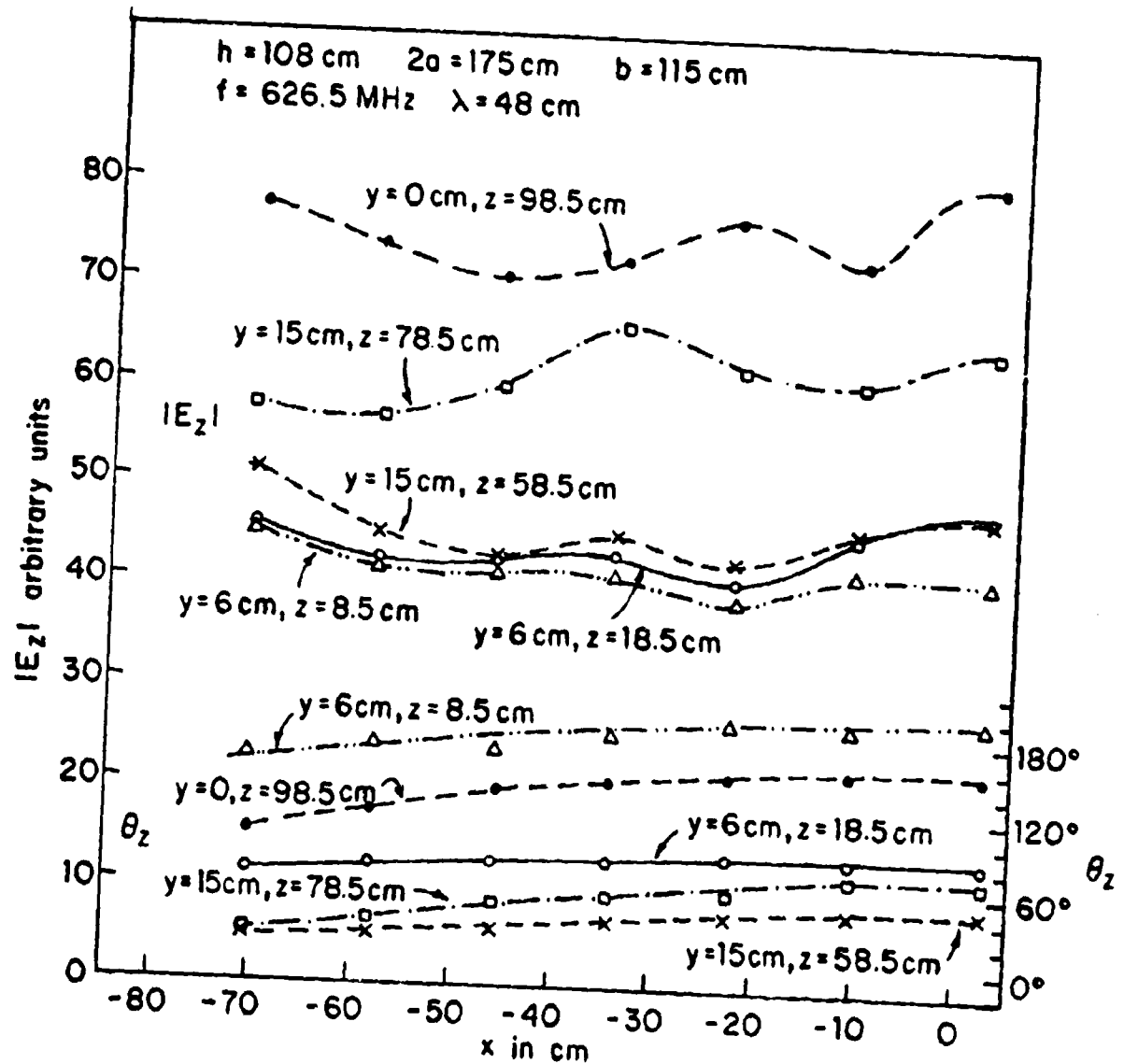h=108 cm, b=114.8 cm, f=626.5 MHz.

59

FIG. 29 MEASURED TRANSVERSE DISTRIBUTION OF E_z

of the fact that the wave fronts are actually spherical and not planar. The value of y selected for each z was the one at the maximum of $|E_z|$ nearest y = 0 in the standing-wave pattern with respect to the longitudinal coordinate y. The graphs of the phases θ_z are like those in Figures 28a, 28b, and 28c.

In Figure 30 are graphs similar to those in Figure 29, but for the smaller height h = 75 cm and the lower frequency 264 MHz. They range from z = 10 cm = 0.09λ from the ground plane to z = 70 cm or h - z = 5 cm = 0.04λ from the top plate. Since only TEM and TM_{01} modes are involved, it is possible also to show a graph of the transverse distribution of E_y at z = 0.5h = 37.5 cm where it is maximum. This is at the bottom of the figure. It is seen that E_y is quite constant from x = 0 to x = -35 cm where it begins to decrease to near half value at x = -87.5 cm, the edge of the upper plate. $|E_z|$ shown at the top is more complicated. Consider first the graph with z = 37.5 cm which shows the TEM mode only since E_z for the TM_{01} mode is zero at z = h/2. E_z as given by this graph is quite constant for -35 cm $\leq$ x $\leq$ 35 cm, but then experiences a significant oscillation. This is due to the spherical wave front which necessarily produces an oscillation along a planar surface. The average magnitude of E_z about which the oscillation takes place decreases from x = 0 outward at each value of z in the range z < h/2 = 37.5 cm; the magnitude increases when z > h/2 = 37.5 cm. As the edge of the upper plate at x = -87.5 cm, z = h = 75 cm is approached, $|E_z|$ increases rapidly and dominates over the relatively small oscillatory amplitude. The changes in $|E_z|$ as x is increased from zero are a consequence of the finite width of the upper plate. The electric lines of E_z that are vertical for infinitely wide plates are pushed outward near the ground plane and converge at and near the edge of the top plate, where there are large concentrations of electric charge on both the lower and upper surfaces, as shown schematically in Figure 31. The thinning of the electric lines near the ground plane corresponds to a reduction in $|E_z|$, the greater density of electric lines near the top plate corresponds to an increase in $|E_z|$.

As pointed out in conjunction with Figure 9(c), the excitation of the parallel-plate section of the simulator by an incident spherical wave provides antisymmetric components H_y of the magnetic field in the xz-plane at y = -b/2 = -57.5 cm. With metal plates of finite width, these can potentially excite antisymmetric $TE_{m\ell}$ modes. A complete analysis of all possible TE

61
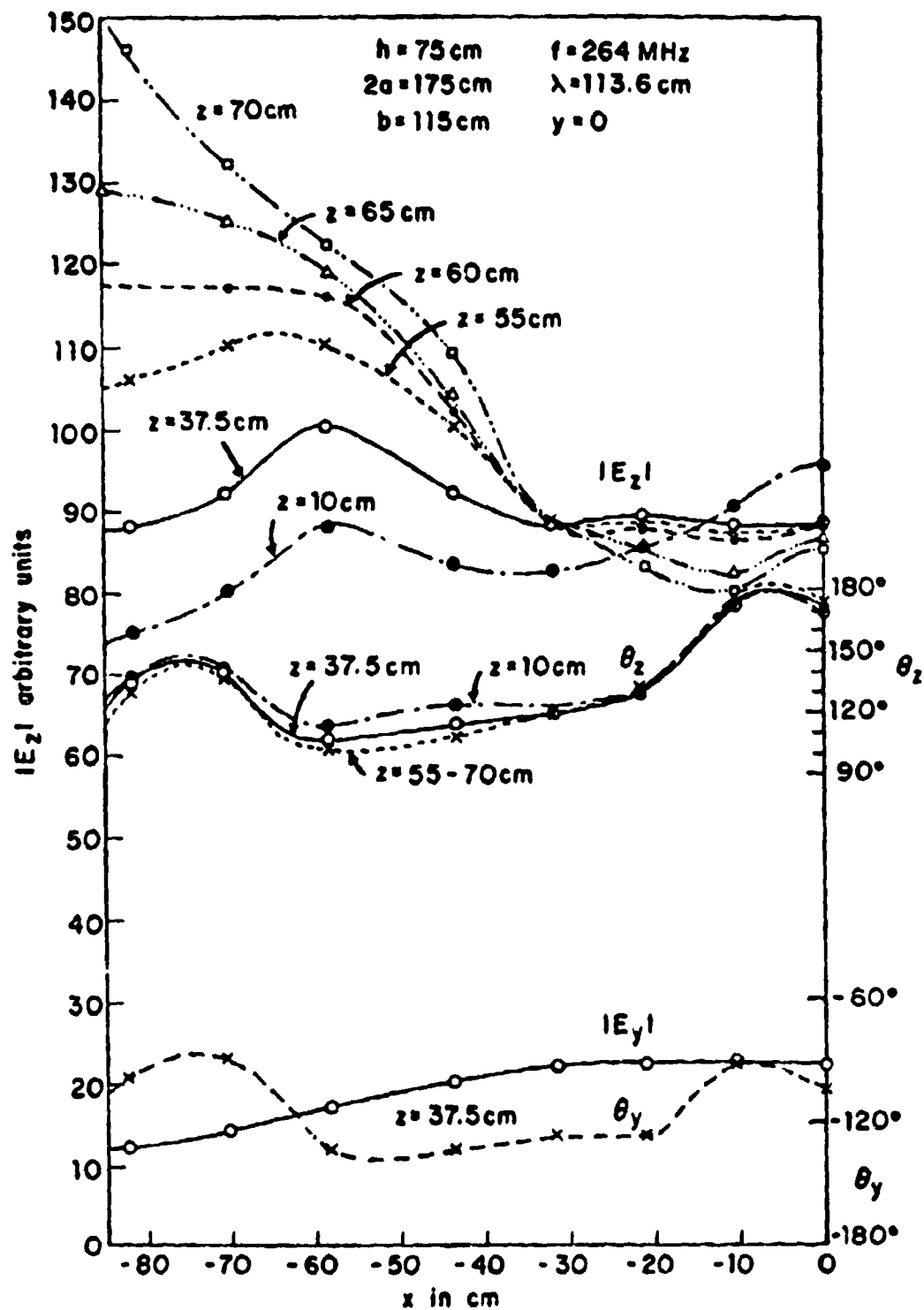
Fig. 30 Transverse distributions of E_z and E_y
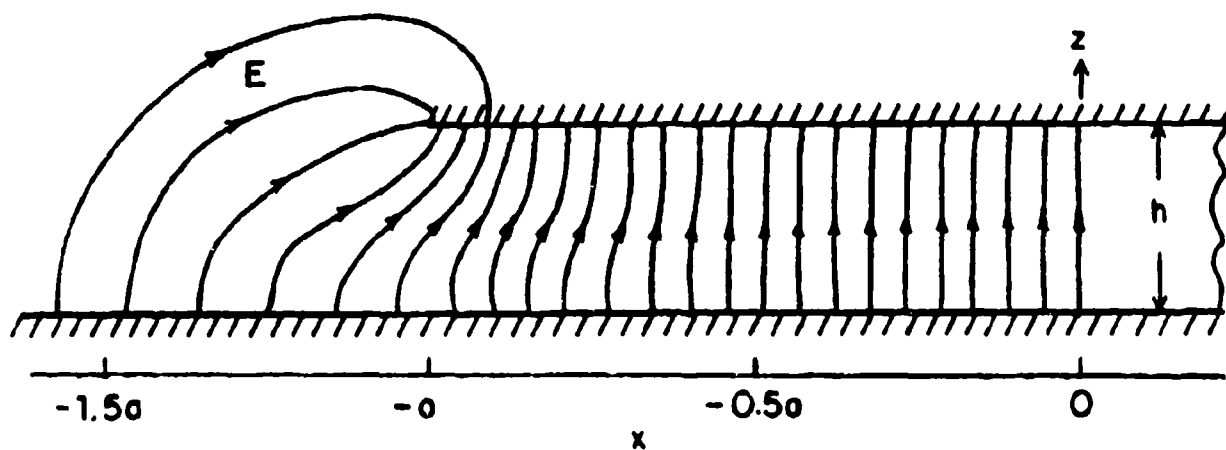
FIG. 31 SCHEMATIC DIAGRAM OF ELECTRIC FIELD LINES IN TRANS-
VERSE PLANE SHOWING FRINGING AT THE OPEN SIDE

modes without reference to any method of excitation has been given by Rushdi et al. (ref. 3). Those of possible interest in the parallel-plate section of the simulator are characterized by the following components of the electromagnetic field. They are antisymmetric in the transverse coordinate x. The antisymmetric $TE_{m\ell}$ modes that can be excited are given by:[*]

$$H_x^a \sim k_{xm\ell} \cos(m\pi z/h)\cos(k_{xm\ell}x) \tag{17}$$

$$H_y^a \sim \cos(m\pi z/h)\sin(k_{xm\ell}x) \tag{18}$$

$$H_z^a \sim (m\pi/h)\sin(m\pi z/h)\sin(k_{xm\ell}x) \tag{19}$$

$$E_x^a \sim (m\pi/h)\sin(m\pi z/h)\sin(k_{xm\ell}x) \tag{20}$$

$$E_z^a \sim k_{xm\ell} \cos(m\pi z/h)\cos(k_{xm\ell}x) \tag{21}$$

where $m = 0, 1, 2, \ldots, \ell = 1, 3, 5, \ldots$. The most important are those with $m = 0$, for which

$$H_x^a \sim k_{x0\ell} \cos k_{x0\ell}x \quad ; \quad H_y^a \sim \sin k_{x0\ell}x \quad ; \quad H_z^a = 0 \tag{22}$$

$$E_x^a = 0 \qquad\qquad ; \quad E_y^a = 0 \qquad\qquad ; \quad E_z^a \sim k_{x0\ell} \cos k_{x0\ell}x \tag{23}$$

with $\ell = 1, 3, 5, \ldots$. Also of possible interest are the $TE_{m\ell}$ modes with $m = 1$, for which

$$H_x^a \sim k_{x1\ell} \cos(\pi z/h)\cos(k_{x1\ell}x) \quad ; \quad E_x^a \sim (\pi/h)\sin(\pi z/h)\sin(k_{x1\ell}x) \tag{24}$$

$$H_y^a \sim \cos(\pi z/h)\sin(k_{x1\ell}x) \qquad ; \quad E_y^a = 0 \tag{25}$$

$$H_z^a \sim (\pi/h)\sin(\pi z/h)\sin(k_{x1\ell}x) \quad ; \quad E_z^a \sim k_{x1\ell} \cos(\pi z/h)\cos(k_{x1\ell}x) \tag{26}$$

---

[*]When referred to the full height with image, h is replaced by 2h, and $m = 0, 2, 4, 6, \ldots$, instead of $0, 1, 2, 3, \ldots$.

64

The amplitudes and wave numbers for the TE modes are given by Rushdi et al. (ref. 3), and normalized amplitudes of the components of the field are evaluated for a parallel-plate region with $h/2a \ll 1$, specifically, $h/2a = 0.01$. This condition is not satisfied by the Harvard simulator, for which $h/2a = 108/175 = 0.62$ or $h/2a = 75/175 = 0.43$. A schematic representation of the TE_{01} and TE_{03} modes is in Figure 32a. It is seen that a superposition of the two modes to give $H_y = AH_{y1} + BH_{y2}$, where B is negative, will roughly approximate the antisymmetric distribution of H_y^{inc} due to the incident spherical wave shown in Figure 9(c). This shows a positive maximum of H_y^{inc} at the right edge of the working volume, a negative maximum of H_y^{inc} at the left edge. Thus, it seems reasonable to suppose that a superposition of $TE_{0\ell}$ modes will approximate the difference $E_z(x,y,z) - E_z(0,y,z)$, where $E_z(0,y,z)$ is the field represented by TEM and TM_{0n} modes, and to assume that the TE_{11} mode shown in Figure 32b and other higher modes contribute negligibly. However, it is obvious from an examination of the distributions in Figure 32a of the TE_{01} and TE_{03} modes that many more than just these two are required to approximate the complicated transverse distributions shown in Figures 29 and 30. In this connection, it is well to note that the actual $TE_{0\ell}$ distributions for a parallel-plate waveguide of finite width as formulated by Rushdi et al. (ref. 3) take full account of the effects of the open sides of the waveguide. For the purposes of this report, the representation of the electromagnetic field in terms of TEM and TM_{0n} modes is adequate without the addition of a sum of $TE_{0\ell}$ modes. As seen from Figures 29 and 30, the departure of $E_z(x,y,z)$ from $E_z(0,y,z)$ is quite small - of the order of 8% - in the central part of the simulator.

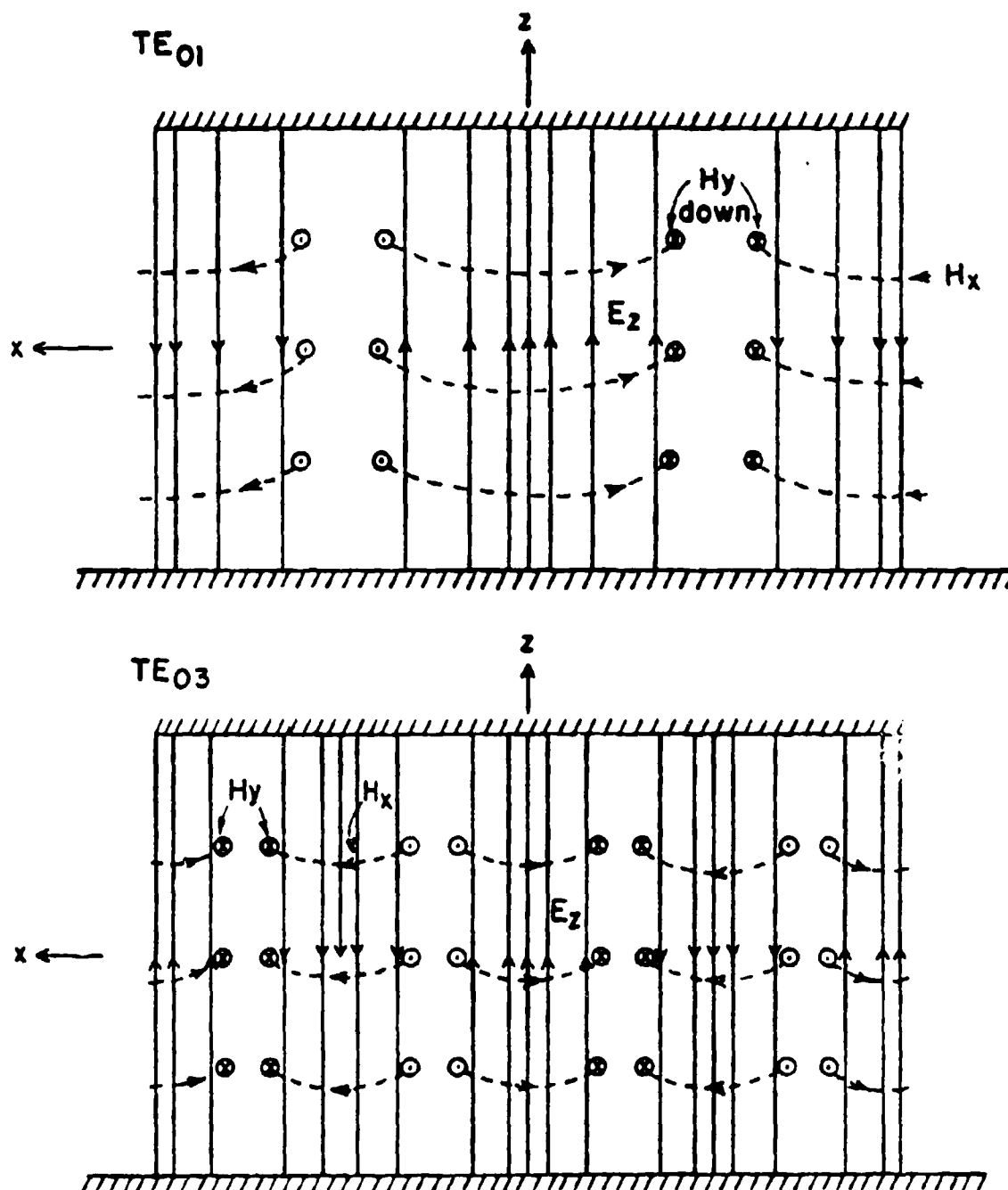FIG. 32a SCHEMATIC DIAGRAM OF TE_{01} AND TE_{03} MODES IN WORKING VOLUME; SOLID LINES, ELECTRIC FIELD E_z; BROKEN LINES, MAGNETIC FIELD $\hat{H} = \hat{x}\,H_x + \hat{y}\,H_y$.
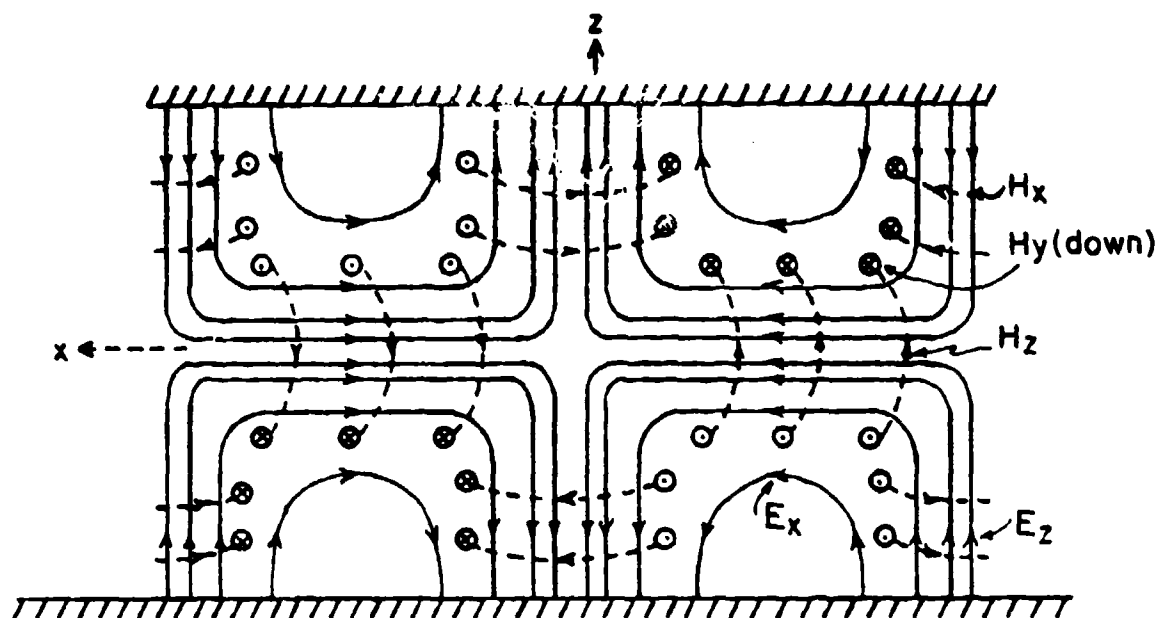
FIG. 32b SCHEMATIC DIAGRAM OF TE$_{11}$ MODES IN WORKING VOLUME.
SOLID LINES, ELECTRIC FIELD; BROKEN LINES, MAGNETIC FIELD.

SECTION IX

THE ACTUAL ELECTROMAGNETIC FIELD IN THE SIMULATOR AS AN APPROXIMATION OF A PLANE WAVE

The electromagnetic field which is to be approximated in the working volume of the simulator is a plane wave traveling in the positive y-direction with the components $E_z(y,t) = E_z(0)e^{i(ky - \omega t)}$, $H_x(y,t) = E_z(y,t)/\zeta_0$, where $\zeta_0 = (\mu_0/\epsilon_0)^{1/2} = 120\pi$ ohms. The field is independent of the transverse coordinates x and z, and is distributed as shown in the upper left of Figure 11 at the instant t = 0. As time passes, the entire pattern moves in the positive y-direction with the speed $c = 3 \times 10^8$ m/sec.

The actual field in the parallel-plate section of the simulator is a spherical wave originating at the driving-point on the ground plane and modified by superimposed reflections from the top plate. The field can be approximated by a sum of appropriate parallel-plate modes, but this is merely a change in the representation and not in the nature of the field. Moreover, all of the modes are generated by the incident field and not by reflection at the load end.

As the cylindrical wave travels in the parallel-plate region, it experiences reflections at the edges $x = \pm a$ and at the end $y = b/2$. The former maintain the transverse standing waves shown in Figures 29 and 30, the latter the longitudinal standing waves shown in Figures 13 and 27. They can be decomposed into separate standing waves of the TEM and TM_{0n} modes, as shown in Figures 23 and 27. These graphs illustrate the standing-wave patterns of E_z and E_y. Measurements were also made of the standing-wave pattern of the magnetic field over a wide range of frequencies centering on f = 264 MHz with h = 75 cm. Selected graphs at f = 250, 264, and 270 MHz are shown in Figure 33. It is seen that as the frequency is varied, the entire standing-wave pattern moves. Simultaneously, the standing-wave ratio fluctuates. Note in Figure 33 how the depth of the minimum varies as its location moves. If the loop probe is fixed at y = 0.074b = 8.5 cm, which locates the minimum for f = 264 MHz shown in the middle figure in Figure 33, and the frequency is then varied, the graph shown in Figure 34 is obtained. This shows a succession of minima that occur at y = 0.074b at different frequencies, but with that at f = 264 MHz the deepest and sharpest. The
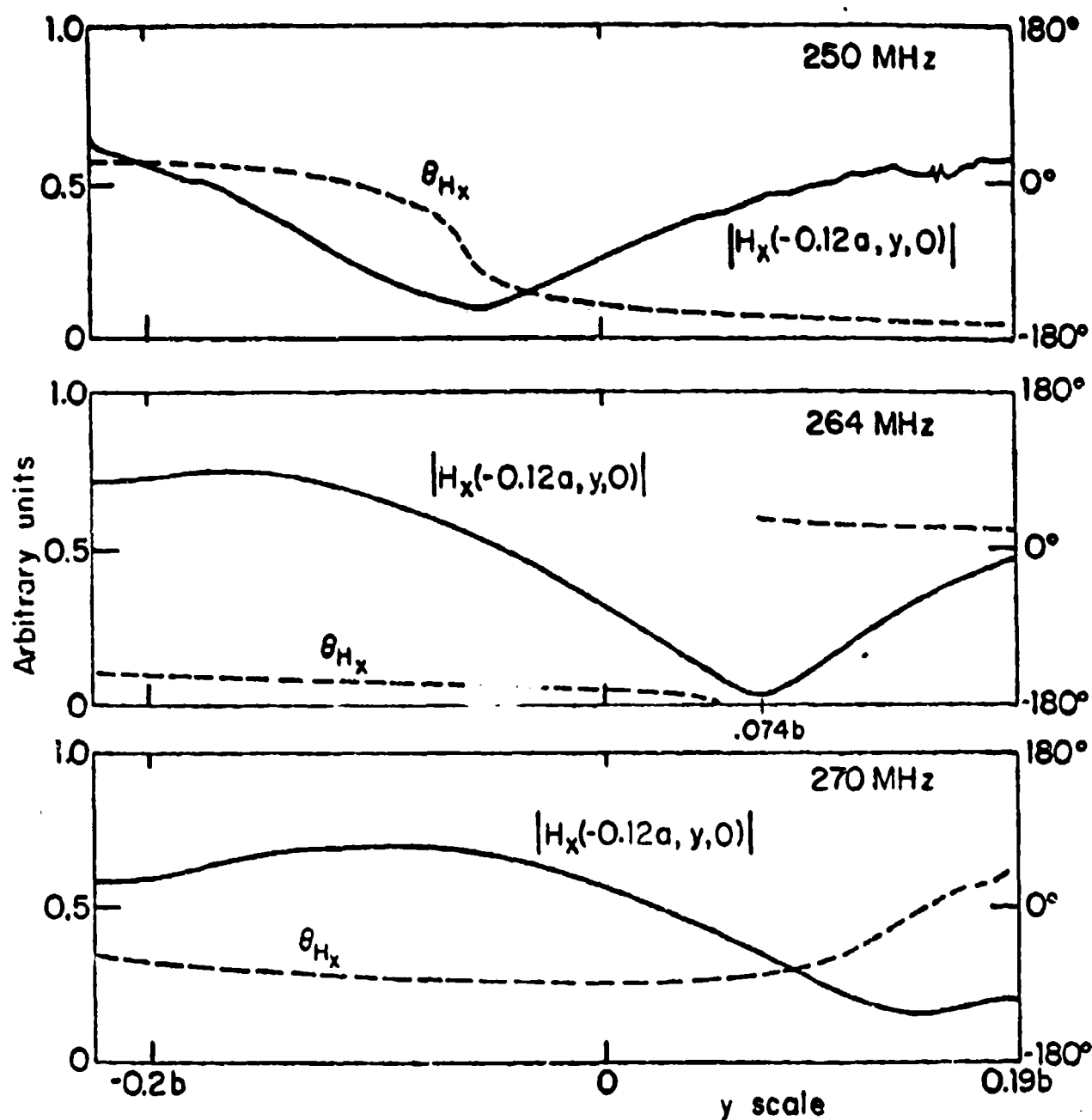
Fig 33 Measured magnitude and phase of the transverse component of
the magnetic field on the ground plane in the working volume; width
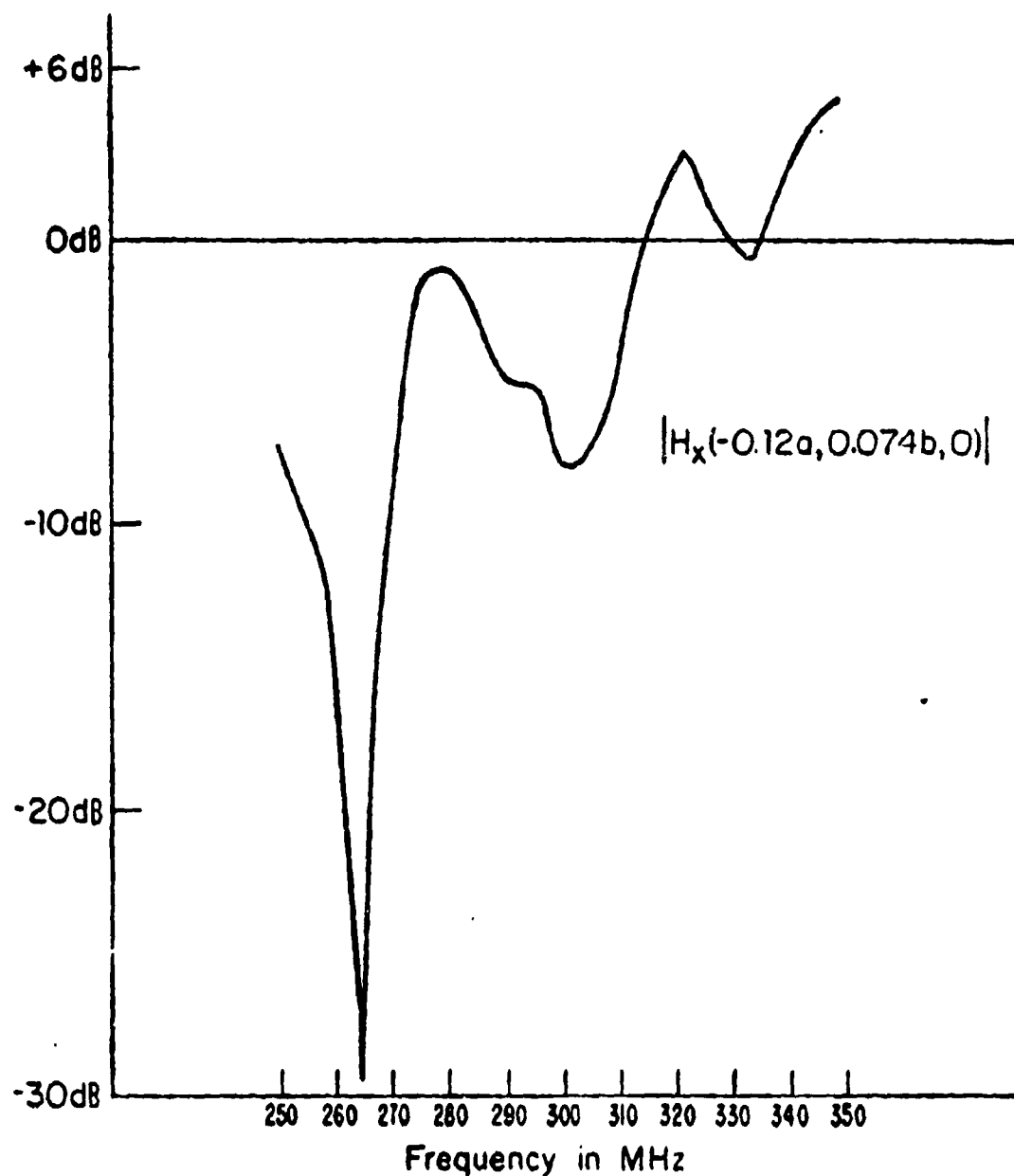$2a = 175$ cm, length $b = 114.8$ cm, height $h = 75$ cm.

Fig. 34 Measured magnitude of the transverse magnetic field at a fixed position in the working volume as a function of frequency; $2a = 175\,cm$, $b = 114.8\,cm$, $h = 75\,cm$, $p_f = 40\,w$

maxima and minima in Figure 34 are a consequence of the standing waves generated in the working volume by reflections of the field at the ends y = ±b/2 and the adjacent tapered sections. The standing-wave ratio varies somewhat with frequency so that the minimum amplitude at any fixed point increases and decreases with frequency. The deepest minimum at y = 8.5 cm occurs at f = 264 MHz. At another location of the probe, the frequency for and the depth of the minimum will be different.

The differences between the actual electromagnetic field in the working volume of the model simulator and a traveling plane wave are significant when h = 108 cm = 2.25λ with f = 626.5 MHz, and considerably larger when h = 75 cm = 0.66λ with f = 264 MHz. In the first place, the component E_z of the electric field is not uniform in either the transverse or vertical directions; secondly, there is a component E_y; and thirdly, there is a significant standing wave. It follows that the electrical environment of a metallic obstacle placed in the working volume is necessarily quite different from what it would be if it were exposed to an incident plane wave. There- fore, it must be expected that currents and charges induced on the surface of an obstacle may also be quite different. A detailed comparison of the distributions of induced currents and charges on obstacles when in the simulator and when exposed to a plane wave is not yet available. However, a sample set of measurements has been made of the very sensitive charge density distribution on the surface of a tubular cylinder with electrical length kh = 3.5π and electrical radius ka = 1 when located at the center of the parallel-plate section of the Harvard simulator with h = 108 cm and f = 626.5 MHz. This means that the axis of the cylinder is at a distance of 7.7λ from the source. Available from earlier measurements at the same frequency are the distributions of charge density along the same cylinder when illuminated by an incident spherical wave from a monopole at a distance of 7.5λ over an open ground plane. Theoretically determined distributions (ref. 8) are also available. The measured magnitudes of the charge density η are shown in Figure 35 for the simulator. in Figure 36 for the incident spherical wave. The theoretical distributions for an incident plane wave are in Figure 37. A comparison of the three figures shows that the general standing-wave nature of the distributions in both the longitudinal and trans- verse directions are comparable, but with significant differences in detail. These are most apparent in the relative magnitudes of the three standing-wave

71
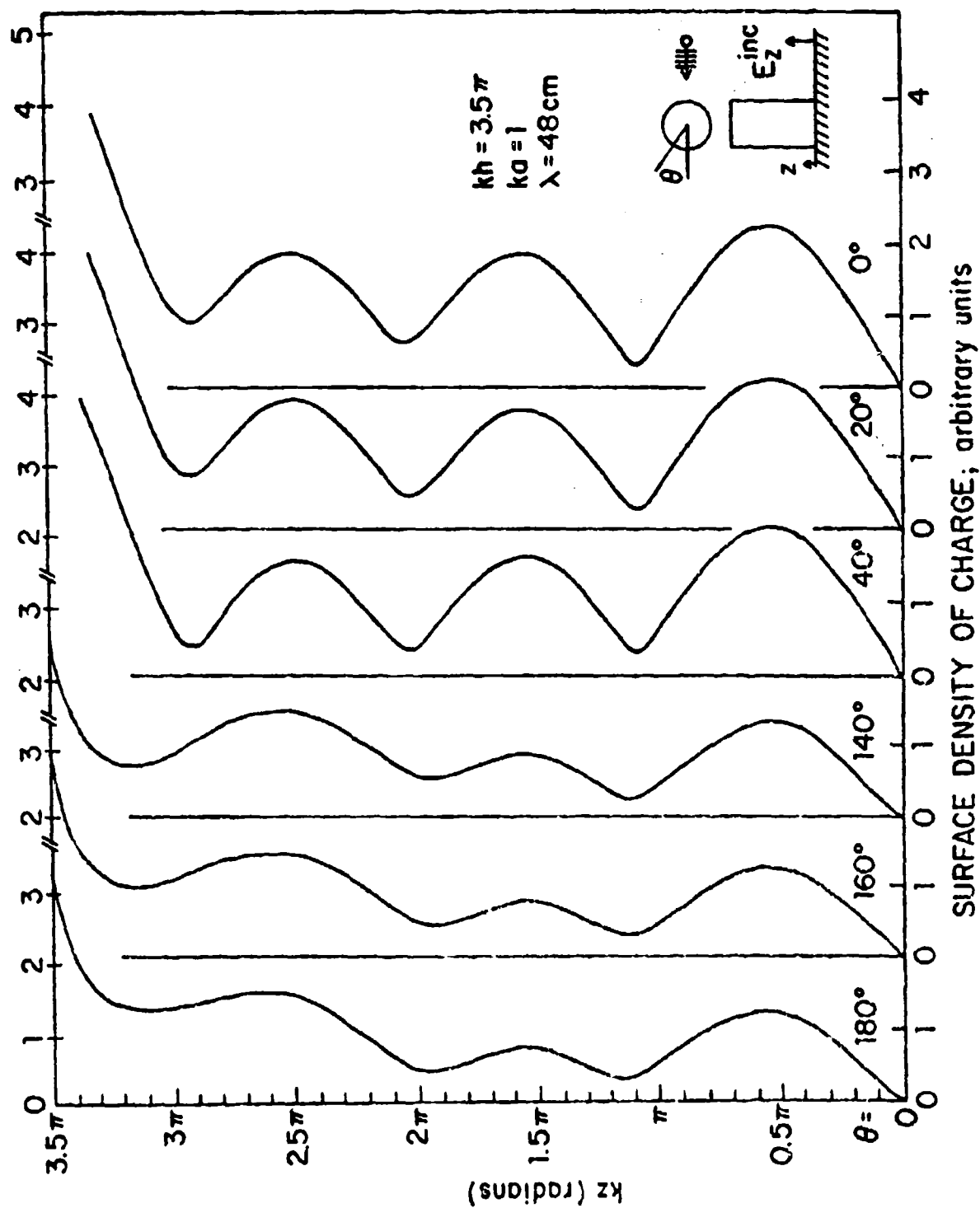
FIG. 35 MEASURED SURFACE DENSITY OF CHARGE ON TUBULAR CYLINDER
IN SIMULATOR

$kh = 3.5\pi$
$ka = 1$
$\lambda = 48cm$

E_z^{inc}

SURFACE DENSITY OF CHARGE; arbitrary units
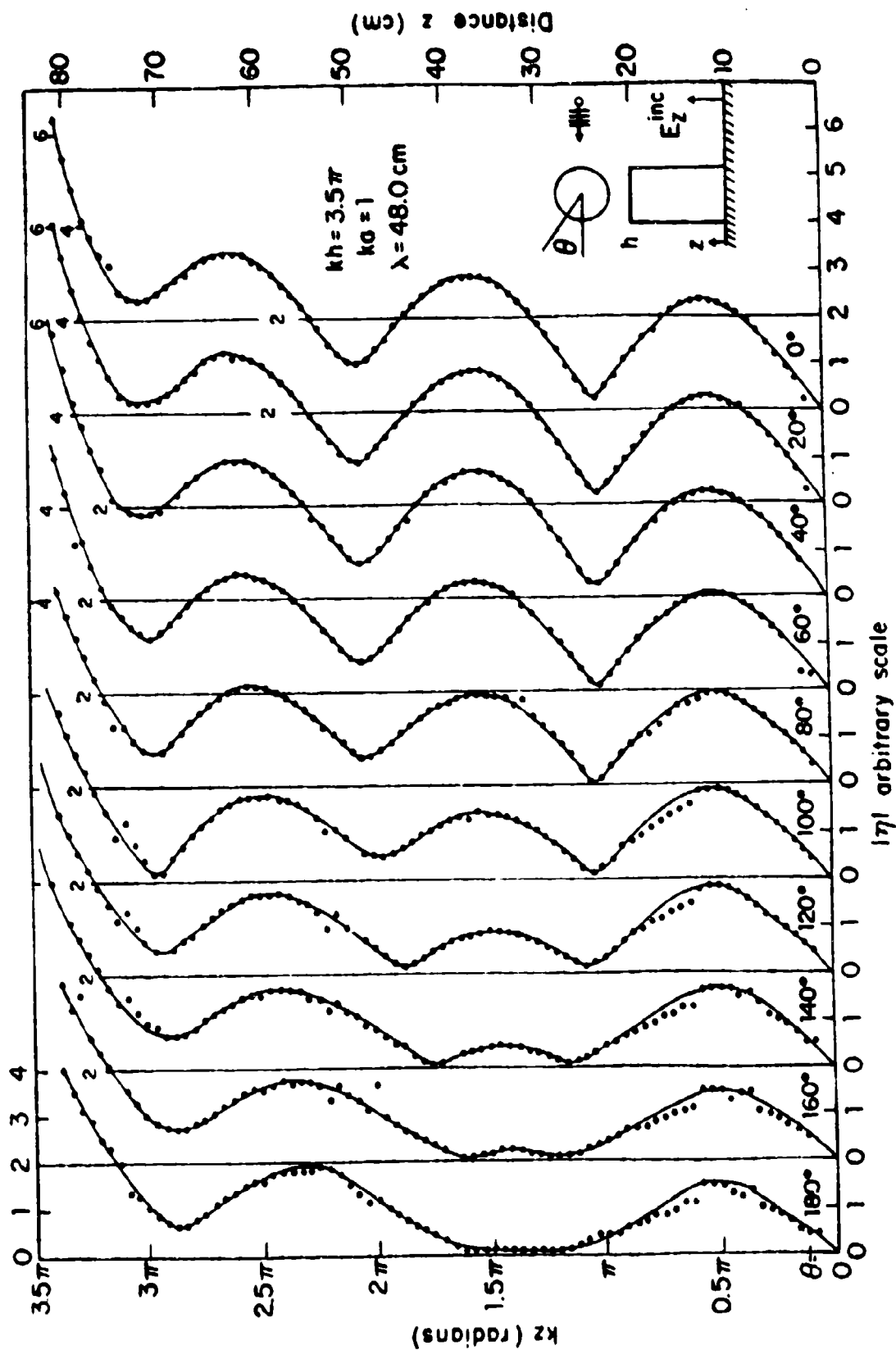
kz (radians)

72

Fig. 36 Measured magnitude of surface density of outside charge on tubular cylinder; E-polarization, normal incidence.
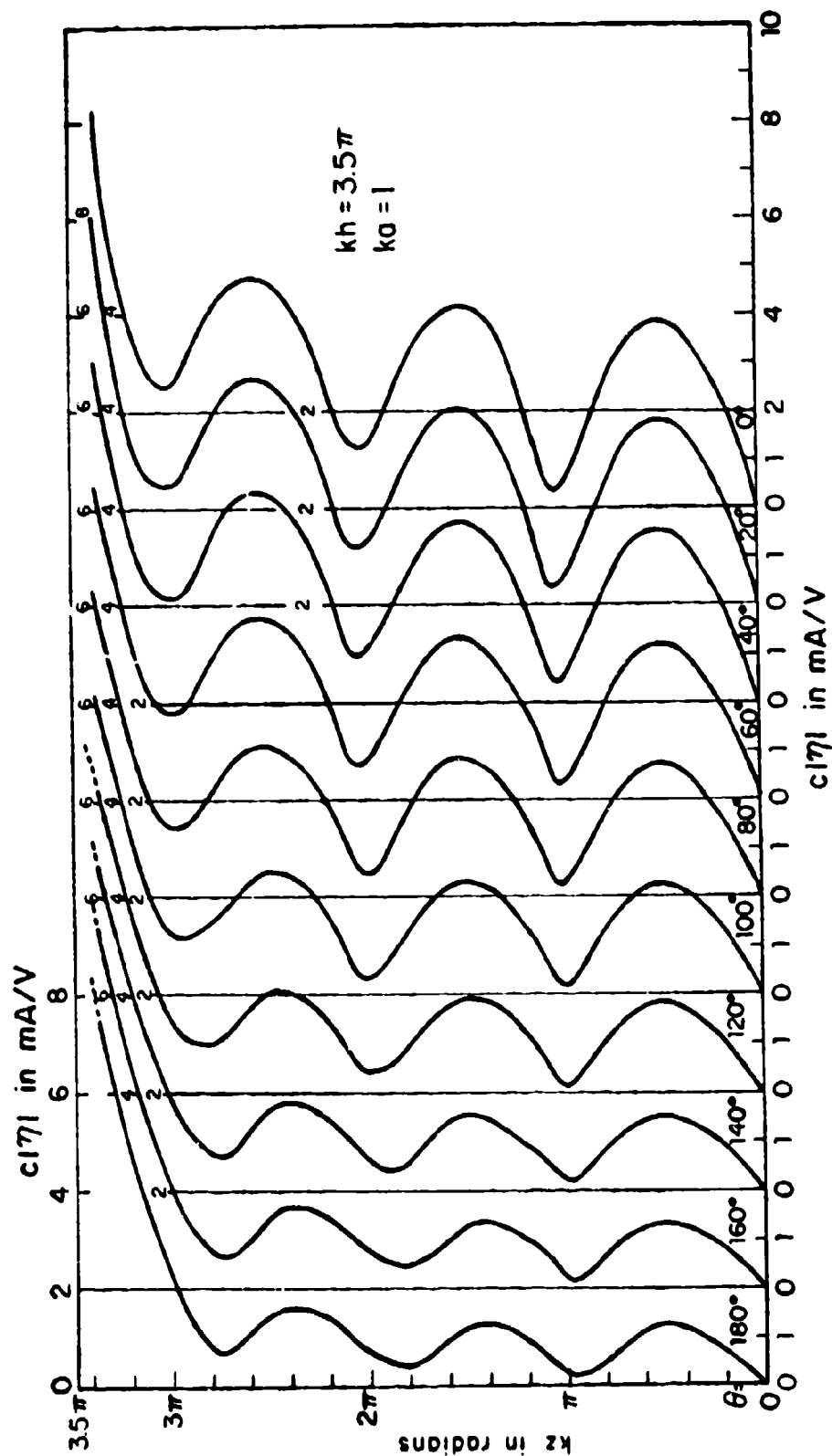
73

Fig. 37 Theoretical magnitude of surface density of outside charge on tubular cylinder; E-polarization, normal incidence.

maxima which occur near $kz = \pi/2$, $3\pi/2$, and $5\pi/2$. These are listed side by side in Table 2 for ready quantitative evaluation. Thus, on the illuminated side ($\theta = 180°$) the theoretical curve has maxima that increase from the ground plane ($z = 0$) upward in the proportions $1.00:1.04:1.27$; the measured values for the simulator are $1.00:0.63:1.29$; and those for the spherical wave are $1.00:0.08:1.23$. Evidently, the second maximum is substantially lower in the simulator and almost completely absent with the spherical wave. It has been shown (ref. 8) that the virtual disappearance of the second maximum with an incident spherical wave is due to the presence of a component of the electric field perpendicular to the surface of the cylinder when the incident wave form is spherical instead of planar. The amplitude and phase relations are such that the second maximum is greatly reduced, the first and third somewhat increased. When the cylinder is in the simulator, the second maximum is reduced but much less than with the spherical wave. This is readily understood since the incident field in the simulator is a spherical wave modified by reflections from the top plate which act to reduce the curvature of the spherical wave.

On the shadowed side ($\theta = 0°$), the ratio of maxima (normalized to the first maximum at $\theta = 180°$) are for the plane wave $3.03:3.25:3.70$; for the simulator $1.71:1.47:1.50$; and for the spherical wave $1.61:1.97:2.23$. Thus, both measured sets have substantially lower charge maxima in the shadow region than required by plane-wave theory. The maxima for the cylinder in the simulator decrease from the ground plane upward, those for the spherical wave and the plane wave increase substantially. Since the distributions on the shadowed side of the cylinder involve the excitation of the entire cylinder with rotational and axial resonance effects both active, it appears that the overall effect of the field in the simulator in inducing charges is less like that of a plane wave than that of the traveling spherical wave. This may be a consequence of the longitudinal standing waves in the simulator, although these have a standing-wave ratio of less than 2 when $h = 2.25\lambda$.

In the absence of more complete information on more complicated obstacles and especially those that have greater lateral dimensions, general conclusions about the adequacy of the field in the simulator are not possible. However, the measured data on an electrically long and thick cylinder do indicate

TABLE 2

RELATIVE MAXIMA OF CHARGE DENSITY ON CYLINDER WITH $ka = 1$, $kh = 3.5\pi$

THEORY FOR PLANE WAVE; MEASURED IN SIMULATOR; MEASURED WITH SPHERICAL WAVE

Max. Near	Illuminated Side						Shadowed Side					
	$\theta = 180°$			$140°$			$40°$			$0°$		
$kz =$	Theory	Simul.	Spher.	Theory	Simul.	Spher.	Theory	Simul.	Spher.	Theory	Simul.	Spher.
2.5π	1.27	1.29	1.23	1.38	1.19	1.12	3.40	1.32	1.97	3.70	1.50	2.23
1.5π	1.04	0.63	0.08	1.23	0.73	0.31	2.90	1.32	1.80	3.25	1.47	1.97
0.5π	1.00	1.00	1.00	1.18	1.08	1.12	2.77	1.64	1.50	3.03	1.71	1.61

that the field in the simulator is sufficiently like that of a plane wave to produce the same general pattern of three-dimensional standing waves of charge density. The relative maxima and minima are observed substantially at the same locations as for a plane wave. However, the relative amplitudes of the individual maxima range from very close agreement to differences by factors up to 2.5. Extensive measurements on electrically thick cylinders have indicated that the distribution of the induced surface density of charge is more sensitive to the nature of the incident wave front than is the distribution of the induced surface density of current.

SECTION X

POSSIBLE METHODS TO IMPROVE THE FIELD IN THE SIMULATOR AS AN APPROXIMATION
OF A TRAVELING PLANE WAVE

The lateral and vertical nonuniformity of the field in the simulator on
the one hand and the existence of standing waves on the other hand constitute
the principal departures from the desired traveling plane wave. Of these the
first is a consequence of the spherical wave fronts that are incident on the
parallel-plate section, the second is due to reflections at and beyond the
junction of the parallel-plate region and the tapered section leading to the
terminating impedance.

It might be supposed that the nonuniformity in the transverse distribu-
tion of the electric field is a problem only at high frequencies when modes
other than the TEM can propagate in the parallel-plate section. The cut-off
wavelength for the TM_{01} mode is λ_{c1} = 2h so that at all wavelengths longer
than 2h, only the TEM mode can propagate. However, with the length b (= 115
cm) of the parallel-plate section substantially less than 2h (= 216 cm or
150 cm) and therefore less than λ when this is greater than 2h, even nonprop-
agating modes may have significant amplitudes in the electrically rather
short parallel-plate section. The obvious way to reduce the transverse
variation in E_z in the parallel-plate section is to provide an incident
field that more nearly approximates a plane wave than does the actual spheri-
cal wave. With the geometry of the input structure predetermined, this is
not readily accomplished. It involves a modification of the phase velocity
of the spherical wave in the tapered section from the generator by some kind
of a collimating lens or its equivalent in the form of metal plates or
corrugations on the ground plane so that the spherical wave front becomes
more nearly planar as it reaches the parallel-plate section.

The existence of standing waves in the parallel-plate section is a
consequence of the fact that the entire structure has the characteristics of
a terminated transmission line only at low frequencies for which the
condition $2\pi h/\lambda \ll 1$ is satisfied. This condition underlies the theory of
all open transmission lines. It requires that radiation be negligible in
determining the characteristics of the line. When it is satisfied, it is
possible to design the transmission line so that virtually all of the power

supplied by the generator is transmitted along it to a matched load at the end. As the height h is increased, radiation becomes significant and, for sufficiently large values of h, dominant. The structure then acts like a traveling-wave antenna. Since the standing-wave ratio in the parallel-plate section is reasonably constant (see Figure 13), it is evident that the effective load on the open parallel-plate waveguide is at or beyond its junction with the sloping triangular plate at the load end. That is, most of the radiation takes place during reflection at or beyond the discontinuity formed by this sharp junction. (It is to be expected that radiation also takes place at the junction of the sloping triangular plate with the parallel plate at the generator end, but this does not affect the standing-wave ratio in the parallel-plate region.)

It is seen from Figure 23 that the amplitudes of the TEM and TM_{01} modes are about equal and those of the TM_{02} and TM_{03} modes negligible when h = 2.25λ = 108 cm with f = 626.5 MHz. In this case, the standing-wave ratio as obtained from Figure 13 is less than 2. On the other hand, Figure 27 shows that the amplitude of the TEM mode greatly exceeds that of the TM_{01} mode when h = 0.66λ = 75 cm with f = 264 MHz, and that in this case the standing-wave ratio is about 3. It, thus, appears that the standing-wave ratio in the working volume can be reduced significantly only by reducing the reflection at y $\geq$ b/2 of the entire component E_z of the electric field between the parallel plates. The selective reduction of the TM_{0n} modes by attenuating E_y, even if 100% successful, would not significantly reduce the standing-wave ratio when it is greatest. There is no comparable way to attenuate separately the $TE_{0\ell}$ modes since they have only an E_z component of the electric field. What is required to reduce the standing-wave ratio is a more frequency-independent termination for the parallel-plate section of the simulator than is provided by the sloping triangular plate with its resistive termination that is frequency independent only at sufficiently low frequencies. This is important primarily in the intermediate range of frequencies when h is of the order of a wavelength, and the standing-wave ratio is highest.

Recent measurements have shown that the very high standing-wave ratio shown in Figure 33 for the magnetic field at f = 264 MHz is reduced from about 20 to near 2 when the terminating resistance of the simulator is

greatly increased from the characteristic resistance of 80 ohms to between 600 and 800 ohms. It is to be anticipated that this change must increase the standing-wave ratio at very low frequencies, at which the simulator behaves like a nonradiating transmission line rather than like an antenna. Measurements at lower frequencies to verify this must be made. A systematic study is then in order to determine the optimum termination from the point of view of the entire frequency spectrum involved.

REFERENCES

1. SooHoo, K. M., "Numerical Analysis of a Transmission-Line EMP Simulator," Sensor and Simulation Note 209, 1974.

2. Dudley, D. G., and Quintenz, J. P., "Multi-Modal Transient Excitation Effects in an Infinite Parallel-Plate Waveguide," Canadian Jour. Physics, 50, pp. 2826-2835, 1972.

3. Rushdi, A. M., Mendez, R. C., Mittra, R., and Lee, S. W., "Leaky Modes in Parallel-Plate EMP Simulators," IEEE Trans. Electromagn. Compatib., EMC-20, pp. 443-453, 1978.

4. Marin, L., "Modes on a Finite Width, Parallel-Plate Simulator, I. Narrow Plates," Sensor and Simulation Note 201, 1974.

5. Marin, L., "Modes on a Finite Width, Parallel-Plate Simulator, II. Wide Plates," Sensor and Simulation Note 223, 1977; Revised, November 1977.

6. Marin, L., and Lewis, Jr., G. C., "Modes on a Finite Width, Parallel-Plate Simulator, III. Numerical Results for Modes on Wide Plates," Sensor and Simulation Note 227, 1977.

7. Marcuvitz, N., Wave Guide Handbook, McGraw-Hill Book Co., New York, 1951, p. 64.

8. Burton, R. W., King, R. W. P., and Blejer, D. J., "Surface Currents and Charges on an Electrically Thick and Long Conducting Tube in E- and H-Polarized, Normally Incident, Plane-Wave Fields," Radio Science, 13, pp. 75-91, 1978, Figure 16.

LIST OF PERSONNEL WHO PARTICIPATED IN RESEARCH

Professor Tai Tsun Wu, Principal Investigator

Professor Max Krook, Co-Principal Investigator

Professor Ronold W. P. King, Emeritus, Senior Scientist

Dr. Tapan K. Sarkar, Post-Doctoral Research Fellow

Mr. Dennis J. Blejer, Research Technician

Mr. S.-K. Wan, Research Technician

Mr. Mark J. Miller, Research Technician

Mr. J. E. Baum, Research Technician

Ms. M. Owens, Staff Assistant

Ms. B. H. Sandler, Programmer & Mathematician

LIST OF PUBLICATIONS

Papers to be Published:

"The Electromagnetic Field in an EMP Simulator at a High Frequency," by
R. W. P. King and D. J. Blejer, scheduled to appear in IEEE Trans. on
Electromagn. Compatibility, August 1979.

"Surface Currents and Charges on a Cross Formed by an Electrically Thick
Cylinder and a Flat Plate in a Normally Incident, Plane-Wave Field," by
R. W. P. King, D. J. Blejer, and R. W. Burton, scheduled to appear in
Radio Science, September-October 1979.

"Current Induced on Single and Crossed Electrically Short and Thin
Tubular Cylinders by a Normally Incident, Plane Electromagnetic Wave,"
by R. W. P. King, D. J. Blejer, and B. H. Sandler, scheduled to appear
in the IEEE Transactions on Antennas and Propagation, September 1979.

Talks Presented:

"Current Induced on Single and Crossed Electrically Short and Thin Tubes
by a Normally Incident, Plane Electromagnetic Wave," by R. W. P. King,
D. J. Blejer, and B. H. Sandler, presented at the 1978 USNC/URSI Meeting,
held at the University of Maryland, College Park, May 15-19, 1978.

"Measured Electric Fields in a Model Simulator," by D. J. Blejer and
R. W. P. King, presented at the 1978 Nuclear EMP Meeting, held at the
University of New Mexico, Albuquerque, June 6-8, 1978.

Interim Reports Issued:

"Currents and Charges on Cylinders in a Parallel-Plate Transmission Line:
Description of Experimental Setup and Sample Measurements," by T. T. Wu,
R. W. P. King, D. J. Blejer, and S.-K. Wan, AFOSR-76-3073 Annual Report,
July 31, 1977.

". Electric Field in a Parallel-Plate EMP Simulator: Theoretical and
Experimental Results," by M. Krook, R. W. P. King, D. J. Blejer, T. K.
Sarkar,   S.-K. Wan, AFOSR-76-3073 Annual Report, July 31, 1978.